Geoscience Frontiers 17 (2026) 102179

Contents lists available at ScienceDirect

Geoscience Frontiers

journal homepage: www.elsevier.com/locate/gsf

Research Paper

Carbon enrichment processes in the oceanic upper mantle preserved in peridotites from Sal Island (Cape Verde)

Andrea Maffeis [a], Maria Luce Frezzotti [a,*], Rosario Esposito [a], Marco G. Malusà [a], Alessandro Aiuppa [b], Andrea Luca Rizzo [a,c], Simona Ferrando [d,e]

[a] Dipartimento di Scienze dell'Ambiente e della Terra , Università di Milano Bicocca, Piazza della Scienza 4, Milano, Italy
[b] Dipartimento di Scienze della Terra e del Mare, Università di Palermo, Via Archirafi, 22 Palermo, Italy
[c] Istituto Nazionale di Geofisica e Vulcanologia, Sezione di Milano, Via Alfonso Corti 12, 20133 Milano, Italy
[d] Dipartimento di Scienze della Terra, Università di Torino, via Valperga Caluso 35, Torino, Italy
[e] Consiglio Nazionale delle Ricerche – Istituto di Geoscienze e Georisorse (CNR-IGG), Sezione di Torino, via Valperga Caluso 35, 10125 Torino, Italy

ARTICLE INFO

Article history:
Received 9 May 2025
Revised 12 September 2025
Accepted 5 October 2025
Available online 8 October 2025

Keywords:
Carbon cycle
Ocean Islands
Lithospheric mantle
Mantle metasomatism
Silicate-carbonate metasomatic melt

ABSTRACT

This study investigates the petrological and metasomatic processes that lead to carbon enrichment in peridotites from Sal Island, Cape Verde. Geochemical and mineralogical analyses reveal a heterogeneous lithospheric mantle, consisting of harzburgites showing ultrarefractory compositions indicative of 20%–40% melting degrees, as well as fertile spinel lherzolites. Evidence of metasomatism is demonstrated by the formation of reaction coronae around dissolving orthopyroxene, consisting of olivine, clinopyroxene, spinel, and interstitial phonolitic glass, together with trachytic/phonolitic glass + carbonate (calcite, aragonite, and dolomite) microveins associated with CO_2 fluid-rich melt inclusions (Type I and II) cutting through olivine and orthopyroxene. The widely differing proportions of silicate and carbonate components in inclusions likely reflect heterogeneous trapping of melt/fluid and degassing CO_2. Thermobarometric data indicate equilibration temperatures from 950 to 1060 °C in harzburgites and up to 1200 °C for reaction coronas in harzburgites and lherzolites, with pressures reaching the aragonite stability field (~2.2–3.5 GPa, or 66–106 km depth). These observations indicate the infiltration at the base of the lithosphere of a silicate-carbonate melt enriched in alkalies, Al, and volatiles (Cl, S, F, N, P). In microveins, the silicate glass composition (e.g., K and Ti content) is consistent with experimental partial melts derived from carbonated sediments with a minor addition of a carbonated eclogite. Enrichments in major and trace elements in clinopyroxene in harzburgites and lherzolites suggest at least two significant metasomatic events involving alkali-rich silicate-carbonate melts at the base of the lithosphere, and CO_2-rich fluid, alkali-rich silicate melts in the deep lithosphere, close to pressure conditions of the carbonate ledge. The introduction of recycled carbon into the upper mantle beneath the Cape Verde archipelago likely occurred during the multiple subduction events that affected the region in the half a billion years leading to the Pangea assembly. Major mobilisation of crustal components, generation of carbonate-rich melts, and subsequent lithospheric metasomatism were triggered by the Oligocene thermal perturbation associated with the Cape Verde mantle plume.

1. Introduction

The Earth's mantle contains 10 to 14 times more carbon than all surface reservoirs, playing a pivotal role in regulating the global carbon cycle on the planet over geological timescales (Shcheka et al., 2006; Dasgupta and Hirschmann, 2010; Foley and Fischer, 2017; Miller et al., 2019). Carbon transport and fixation in the upper mantle impact the geophysical properties of the mantle, the onset of mantle melting, and, ultimately, CO_2 volcanic degassing (Gaillard et al., 2008; Frezzotti and Touret, 2014; Hammouda and Keshav, 2015). Changes in the chemical or thermal state of the upper mantle, whether due to subduction, rifting, mantle upwelling, or mantle plumes, can cause the upper mantle to behave as a carbon sink or a significant carbon source (Gibson and McKenzie, 2023). There is a wealth of detailed knowledge on deep carbon processes in the mantle wedge of subduction zone

* Corresponding author.
E-mail address: maria.frezzotti@unimib.it (M.L. Frezzotti).

https://doi.org/10.1016/j.gsf.2025.102179

magmas (e.g., Kelemen and Manning, 2015; Plank and Manning, 2019; Manning and Frezzotti, 2020; Farsang et al., 2021; Maffeis et al., 2023, 2024). Oceanic island basalts (OIBs) are also characterised by enrichment in volatiles, mainly CO_2, and incompatible trace elements and are more oxidised compared to mid-ocean ridge basalts (MORB; Dasgupta and Hirschmann, 2010; Wong et al., 2019; Aiuppa et al., 2021), raising questions on possible carbon enrichment processes in the oceanic upper mantle by plumes, by recycling of ancient subducted oceanic crust and sediments (i.e., long term storage in the upper mantle), and on the role of metasomatic melts in deep carbon transport.

The Cape Verde Archipelago is one of the crucial locations for addressing deep carbon geodynamics in the oceanic upper mantle. Recent research has reported extremely high CO_2 contents (2.0 – 2.7 wt.%) in primitive magmas (DeVitre et al., 2023; Lo Forte et al., 2024a), and relatively large volumes of intrusive and effusive carbonatites are present on six of the ten islands in this archipelago (Doucelance et al., 2010; de Ignacio et al., 2012). According to Sun and Dasgupta (2023), Cape Verde represents a carbon-rich mantle source, and primitive OIB magmas may contain up to 8.8 wt.% and 12.8 wt.% of CO_2 at the source. Several lines of geochemical evidence suggest that this volatile enrichment reflects, at least in part, the contribution of recycled carbon components. Heavy $\delta^{13}C$ values inferred for the primary magma beneath Fogo (Lo Forte et al., 2024b), radiogenic Sr–Pb isotopes in magmas (Doucelance et al., 2010), and recent Ca isotope data from southern Cape Verde islands carbonatites (Amsellem et al., 2020) all support the involvement of subducted carbonate-rich lithologies. At the same time, noble gas compositions in magmas ($^3He/^4He$ up to 15.5 Ra; Mourão et al., 2012) and $\delta^{13}C$ values in northern Cape Verde islands carbonatites (from −8‰ to −4.2‰; Madeira et al., 2010) point to a deep, relatively undegassed source. This combination of signatures indicates a hybrid mantle reservoir (Doucelance et al., 2010; Villaseca et al., 2025) containing both primordial and recycled components.

However, the mechanisms and pathways by which carbon is transferred, stored, and remobilised in the mantle beneath Cape Verde remain an open question. The Cape Verde lithospheric mantle shows anomalous thermal properties and complex seismic profiles (Wilson et al., 2010; Carvalho et al., 2022). Geophysical data reveal a transition from continent-style to ocean-style magnetic anomalies in correspondence with the easternmost island of the archipelago (O'Reilly et al., 2009), which also shows positive anomalies in S-wave velocities in the 100 175 km depth range relative to the mantle tomography model of Begg et al. (2009) (Fig. 1a). A high-velocity seismic anomaly is interpreted either as due to a thick, stable and depleted lithospheric root or due to a thinner thermally rejuvenated mantle (e.g., Lodge and Helffrich, 2006; Vinnik et al., 2012; Carvalho et al., 2019). Mantle peridotite xenoliths from Santo Antão, Santiago, and Sal Islands reveal a heterogeneous lithosphere consisting of variably metasomatised spinel lherzolites and ultra-depleted spinel harzburgites (Ryabchikov et al., 1995; Mendes et al., 2004; Bonadiman et al., 2005; Simon et al., 2008; Martins et al., 2010). At Sal Island, Si-undersaturated ultramafic melts similar to proto-kimberlite melts have been proposed as metasomatic agents (Bonadiman et al., 2005) in the absence of a carbonate component. Conversely, metasomatic carbonates, CO_2, phlogopite, and amphibole are reported in peridotites from the Santiago and Santo Antao Islands (Mendes et al., 2004; Martins et al., 2010).

Therefore, the connections between mantle metasomatic processes, lithosphere refertilisation, and carbon enrichment in the upper mantle need further investigation. In this study, we combine mineral chemistry, thermobarometry, and fluid/melt inclusion analyses on spinel harzburgitic and lherzolitic xenoliths from Sal Island to determine the petrological structure of the lithospheric mantle and identify the carbon-bearing metasomatic agents and mineral assemblages, along with their pressure–temperature conditions. These findings provide new insights into the structure, thermal state, and carbon pathways of the lithospheric mantle beneath Cape Verde, with wider implications for understanding deep carbon cycling in intraplate oceanic environments.

2. Geological setting and previous studies

The ten islands of the Cape Verde archipelago are situated in the central Atlantic off the West African margin. The Moho below the Jurassic-Cretaceous (120 140 Ma) Atlantic oceanic crust varies in depth, ranging from about 13 km beneath Sal Island in the east to about 10 km beneath Brava and Santo Antão Islands in the west (Fig. 1a, b; Lodge and Helffrich, 2006; Vinnik et al., 2012; Carvalho et al., 2019). Onshore along the West African Margin, west-dipping thrust belts such as the Mauritanides and the Rokelides testify to ancient subductions in a region later affected by the opening of the central Atlantic Ocean in the Mesozoic (Fig. 1a).

Although the onset of magmatism is hypothesised to have begun around 40 50 Ma (Mitchell et al., 1983), the oldest outcropping magmatic products on the easternmost Sal Island date around 26 Ma. An increase in activity is recorded from approximately 12 Ma, continuing to the present in the western islands of Fogo and Brava (e.g., Torres et al., 2002; Holm et al., 2008; Barker et al., 2021). This magmatic activity consists of dominant, relatively primitive SiO_2-undersaturated products, including basanites, nephelinites, alkaline basalts, melilites, and tephrite, along with subordinate trachytes and phonolites (e.g., Gerlach et al., 1988; Jørgensen and Holm, 2002; Holm et al., 2006; Torres et al., 2010). Intrusive and effusive carbonatites have been reported on six of the ten islands (i.e., Maio, Santiago, Fogo, Brava, São Nicolau, and São Vicente Islands), dating from 10 Ma to 11 Ma to recently 0.25 Ma at Brava (Holm et al., 2008; Madeira et al., 2010; Barker et al., 2021).

Cape Verde's primitive magma geochemistry suggests mantle partial melting occurring at depths from 60 90 km to 110 135 km or even up to about 150 km: within the garnet stability field (Gerlach et al., 1988; Holm et al., 2006; Torres et al., 2010; Sun and Dasgupta, 2023). Primitive magmas display significant isotopic variability (Fig. 1b), which is interpreted as a result of mixing between HIMU ("high μ," indicating mantle enriched by recycled oceanic crust or carbonates; e.g., Chauvel et al., 1992; Stracke et al., 2003; Castillo, 2015) and a depleted mantle signature, a DMM (Depleted Mid-ocean ridge Mantle; e.g., Hart, 1988; Stracke et al., 2003) component, in the northwestern islands (Santo Antão, São Vicente and São Nicolau). Recent work further emphasises a FOZO (i.e., Focal Zone; Hart et al., 1992) component in the older products of the northern islands (Villaseca et al., 2025 and references therein). Conversely, the southeastern islands (Fogo, Santiago, and Maio) show a mixture of EM1 (Enriched Mantle 1, indicative of a mantle affected by recycled sediments or lower crust material; Hart, 1988; Boyet et al., 2019) and HIMU (Gerlach et al., 1988; Doucelance et al., 2003; Holm et al., 2006; Barker et al., 2010, 2014; Martins et al., 2010; Torres et al., 2010; Mourão et al., 2012b). Additionally, Brava Island shows the evolution of HIMU + DMM components into HIMU-EM1 components over time, and Sal Island shows evidence of HIMU + EM1 + DMM components (Torres et al., 2010; Mourão et al., 2012; Fig. 1b).

Helium isotope systematics (R/Ra up to 12.85) indicate a largely undegassed, lower mantle plume source beneath the Northern Islands (Doucelance et al., 2003; Madeira et al., 2010; Mourão et al., 2012), while a MORB-like mantle beneath the Southern Islands (Doucelance et al., 2003; Lo Forte et al., 2024b). $\delta^{13}C$ values from Cape Verde carbonatites range from −8.0‰ to −4.2‰, consis-

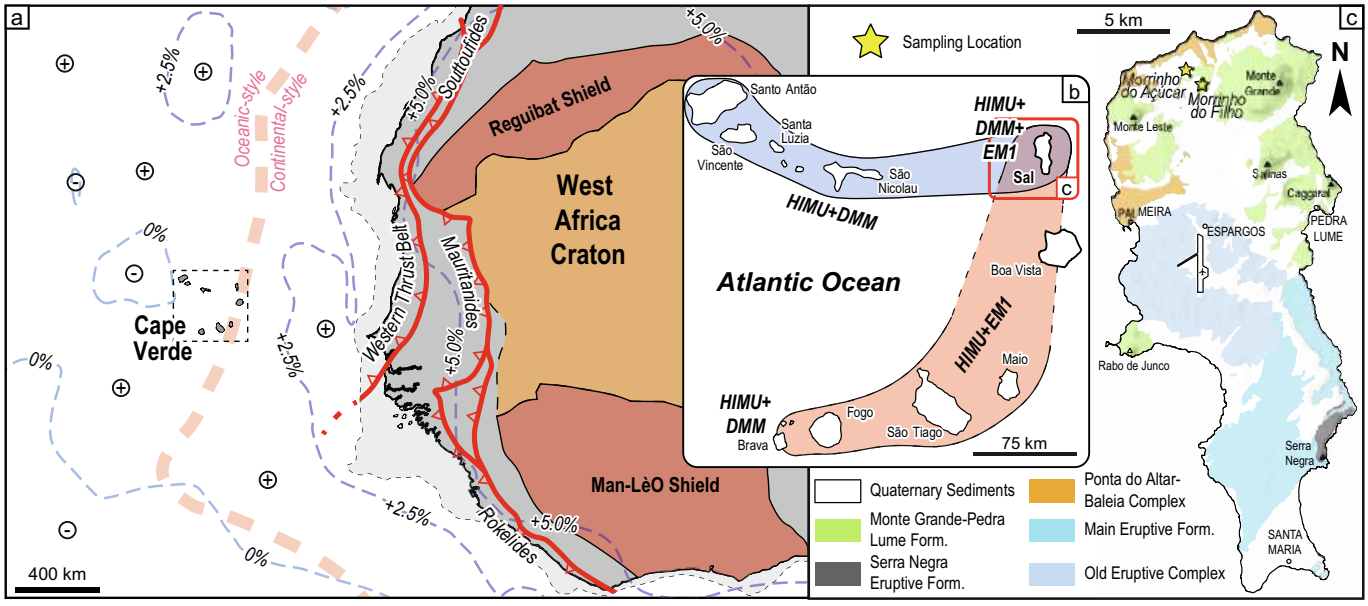

Fig. 1. (a) Regional map showing the position of the Cape Verde Archipelago relative to the nearby West African Craton and related sutures and thrust belts of its western margin. The red dashed line represents the boundary between ocean-style and continent-style magnetic anomalies (redrawn from O'Reilly et al. (2009)), while the thinner dashed blue lines represent contours of percentage variation of Vs (relative to 4.5 km/s) between 100 and 175 km of depth from the mantle tomography model of Begg et al. (2009). The thin dashed black line delimiting the light grey area represents the West African continental shelf. (b) Sketched map of the Cabo Verde Archipelago, with the island's isotopic groupings inspired by Barker et al. (2014) and modified according to Torres et al. (2010), and (c) a simplified geologic map of Sal, with the sampling locations marked by stars. Map modified from Silva et al. (1990). HIMU stands for high μ, DMM stands for Depleted Morb Mantle; EM1 stands for Enriched Mantle 1.

tent with derivation from a deep, non-recycled mantle source (Madeira et al., 2010). In contrast, $\delta^{13}C$ values up to –0.4‰ predicted for primary magma beneath Fogo suggest isotopically heavier carbon (Lo Forte et al., 2024b). Combined with recent light and marine carbonate-like Ca isotope data from southern Cape Verde islands carbonatites (Amsellem et al., 2020), this points to a possible recycled carbonate component in the Cape Verde mantle source. Several studies indicate that the plume beneath Cape Verde is compositionally zoned both laterally and vertically: a more depleted FOZO- and DMM-like domain feeds the northern islands, whereas an enriched, HIMU- and EM1-influenced domain feeds the southern islands (Escrig et al., 2005; Lo Forte et al., 2024b; Villaseca et al., 2025). This compositional heterogeneity likely reflects differential incorporation of ancient recycled components into the plume at depth, as well as variable interaction with the overlying lithosphere during melt ascent.

Peridotite xenoliths from Santo Antão, Santiago, and Sal Islands reveal a heterogeneous lithosphere composed of spinel lherzolites and ultra-depleted spinel harzburgites, equilibrated at temperatures ranging from 930 °C to 1210 °C and pressures between 1.3 GPa and 2.1 GPa near the spinel-garnet transition in the simplified CMAS system (Ryabchikov et al., 1995; Bonadiman et al., 2005). Across the archipelago, peridotites have been variably enriched and refertilised (Mendes et al., 2004; Bonadiman et al., 2005; Simon et al., 2008; Martins et al., 2010). At Sal Island, spinel lherzolites reflect an enriched mantle affected by a very low degree of partial melting (~4%; Bonadiman et al., 2005). Conversely, ultradepleted spinel harzburgites have been interpreted as evidence for a sub-lithospheric, buoyant, ancient, and depleted continental mantle (SCLM), likely of cratonic origin (Bonadiman et al., 2005; Simon et al., 2008; O'Reilly et al., 2009; Coltorti et al., 2010). Most lherzolites show metasomatic processes and refertilisation through the reaction of orthopyroxene and clinopyroxene with ultramafic silicate melts enriched in alkalies and volatiles, similar to protokimberlite melts (Bonadiman et al., 2005). Silicate alkaline glasses and CO_2 fluid inclusions were found in spinel harzburgites from Santo Antão Island (Mendes et al., 2004), while metasomatic carbonates, phlogopite, and amphibole were reported in spinel peridotites from Santiago Island (Martins et al., 2010). Carbonates and hydrous potassic metasomatic phases have not been reported in Sal peridotites.

3. Methods

We used 100-μm-thick sections to study fluid and melt inclusions in peridotite samples selected for the present study. Major and minor elements in minerals and glasses were analysed using a super-probe electron microscope with five-wavelength dispersive spectrometry (WDS) at the Dipartimento di Scienze della Terra "A. Desio", Università degli Studi di Milano. An accelerating voltage of 15 kV combined with a beam current of 5nA and a spot mode was used as instrumental conditions for the mineral phases. The elements analysed were Si, Ti, Al, Cr, Fe, Mn, Mg, Ca, Na, K, Ni, Cl, F and S.

In-situ trace element characterisation of orthopyroxene and clinopyroxene was performed by laser ablation inductively coupled plasma mass spectrometry (LA-ICP-MS; single-detector quadrupole iCAP RQ, Thermo Fisher Scientific) at the Dipartimento di Scienze della Terra "A. Desio", Università degli Studi di Milano. The laser ablation system is an Analyte Excite 193 nm ArF excimer laser microprobe equipped with a HelEx II volume sample chamber for fast washout. Laser spot size ranges from 10 to 40 μm. A laser fluence of 6.0 J/cm^2 and a repetition rate of 10 Hz were used for both standards and unknowns. Ablated particles were transported to the ICP-MS using PTFE tubing with He gas at a flow rate of 0.54 and 0.36 L/min into the sample chamber and the HelEx II cup, respectively. The sample and He mixture were mixed with Ar using a Y-connection before introduction into the ICP-MS. Each spot was analysed for a total of 110 s, which included 40 s of background analysis (comprising 10 s of laser warm-up) and 60 s of laser ablation measuring isotope peak intensity, followed by 10 to 20 s of washout time. The standards used were NIST SRM 612 and USGS

GSD-2 g, which served as external standards and quality controls. Andesitic glass ARM3 (Wu et al., 2019) was used solely for quality control. Data reduction was performed using the Glitter software for recalculations, employing the SiO_2 and CaO values of the analysed phases as internal standards.

Raman spectra on inclusions and glass microveins were acquired with a HORIBA LabRAM HR Evolution Raman System at the Dipartimento di Scienze dell'Ambiente e della Terra, Università degli Studi di Milano-Bicocca. The spectrometer system features an 800 mm focal distance and is coupled with an air-cooled 1024 × 256 pixel CCD detector cooled by the Peltier effect to −70 °C. Single-point analyses have been performed using a linearly polarised solid-state green laser source at 532.06 nm, with a nominal 300 mW output, set to 75 mW using a 25% neutral density filter. Raman spectra acquisition was performed with a backscattered geometry, focusing the laser beam within fluid inclusions to a depth of up to 20 μm beneath the sample surface with a transmitted light Olympus BX41 microscope. A 100X objective with a long working distance was used for all the acquisitions to enhance spatial resolution (≤ 1 μm^3). The confocal pinhole was set to a 100 μm diameter, and a 600 grooves per millimetre grating was adopted, with a fixed accumulation time of 40 s. Raman spectra baseline removal and fitting were performed using Fytik 1.3.1 (Wojdyr, 2010), and spectra fitting was performed with the built-in function PseudoVoigt for both solid and fluid phases. Quantitative analyses of gaseous phases are obtained using the method described by Frezzotti et al. (2012).

4. Petrography

The investigated peridotite samples are from the Island of Sal, sampled in two nephelinitic to basanitic necks (Morrinho do Açúcar and Morrinho do Filho; Fig. 1c) in the island's northern part, dated at 11.23 ± 0.09 Ma (Holm et al., 2008). We collected 43 peridotite xenoliths from the two volcanic necks. As previously documented (Bonadiman et al., 2005, 2011; Shaw et al., 2006), most xenoliths from this locality show evidence of infiltration by the host lava. Consequently, we carefully selected 12 samples that exhibited no lava infiltration at either the sample or micro-scale. Seven samples are spinel harzburgites (SAL1G, SAL3H, SAL1S, SAL3A, SAL2C, SAL3F, SAL3D; Fig. 2a) and five samples are spinel lherzolites (SAL1X, SAL1F, SAL3G, SAL1A, SALE; Fig. 2a).

Protogranular (Mercier and Nicolas, 1975) spinel harzburgites (4 – 8 cm in size) consist of olivine (70% – 86%), orthopyroxene (10 – 28 vol.%), clinopyroxene (traces – 4 vol.%), and spinel (<0.1 – 3.4 vol.%; Table 1; Fig. 2a). Coarse-grained porphyroclastic olivine (Ol_P, 1–10 mm) exhibits a prismatic to equant shape and the presence of kink bands (Fig. 3a). Interstitial olivine neoblasts (< 0.2 mm) are rare. Orthopyroxene porphyroclasts (Opx_P, 1 – 9 mm) have a tabular to equant habit (Fig. 3b), often showing kink bands and clinopyroxene exsolution lamellae in their cores. Clinopyroxene (Cpx_P) is present as tiny and, rarely, as large crystals (0.2 – 2 mm; Fig. 3c). Cpx shows orthopyroxene exsolution lamellae, with one sample showing exsolution lamellae of orthopyroxene and spinel. Rare spinel (Spl_P) occurs as small (<0.1 mm) inclusions within Ol_P or as interstitial holly leaf crystals (reaching up to 0.6 mm) with local and thin spongy rims (Spl_{SPG}); spinel is absent in sample SAL1G.

The petrographic characteristics of lherzolites are similar to those described in previous studies (Bonadiman et al., 2005, 2011). Spinel lherzolites (4 – 8 cm in size) show protogranular (Mercier and Nicolas, 1975) to poikilitic textures and consist of olivine (62 – 68 vol.%), orthopyroxene (22 – 30 vol.%), clinopyroxene (7 – 13 vol.%), and spinel (< 0.1 vol.%; Table 1; Fig. 2a). Olivine porphyroclasts (Ol_P) are large (1 – 3 cm) and show undulose extinction with local kink bands. Ol_P grains are often poikilitic and include orthopyroxene (Opx_P; 0.2 – 3.0 mm) and clinopyroxene (Cpx_P; 0.1 – 2.5 mm; Fig. 2b, c). Rarer Cpx and Opx porphyroclasts are also observed, showing undulose extinction (0.1 – 1.0 mm). Clinopyroxene consistently shows spongy rims (Cpx_{SPG}; Fig. 2d); in one sample, SAL3G, all clinopyroxene is spongy. This feature has been previously interpreted as resulting from partial melting during ascent in the host lava (e.g., Shaw et al., 2006; Bonadiman et al., 2011). Rare spinel is present as small (< 0.1 mm) inclusions in Ol_P but can reach up to 0.5 mm when found as rare interstitial holly leaf crystals with local and thin spongy rims (Spl_{SPG}).

In harzburgites and lherzolites, Opx shows disequilibrium textures and variable resorption and is surrounded by microveins and coronae of variable thickness (Figs. 2c and 3b). Microveins (0.03 – 0.2 mm) rimming Opx are observed in all samples, forming an interconnected intergranular network in rocks. In harzburgites, coronae up to 1.0 mm thick are also observed around relic Opx. Coronae and microveins consist of fine-grained aggregates (0.01 – 0.10 mm) of clinopyroxene (Cpx_M), olivine (Ol_M), spinel (Sp_M), and subordinate glass (Gl_M; Fig. 3d). The metasomatic mineral phases show euhedral to subhedral habits, suggesting equilibrium with the infiltrating melt. Gl_M is always interstitial, suggesting trapping of residual melt following the crystallisation of Ol_M, Cpx_M and Sp_M, but it is frequently altered (Fig. 3d). Fluid and melt inclusions microstructurally associated with microveins and coronae are also observed and reported below. Spongy clinopyroxene occurs far from these domains (Fig. 2d).

5. Fluid and melt inclusions and glass microveins

In olivine and orthopyroxene of harzburgites and lherzolites, fluid and melt inclusions show a distribution pattern in clusters and short trails, typically departing from interstitial metasomatic microveins, and large coronae around Opx. These distributions indicate that olivine and orthopyroxene trapped metasomatic fluids and melts at distinct stages of orthopyroxene destabilisation and reaction.

5.1. Type I – silicate glass – carbonate + CO_2–(CO)–N_2 fluids microveins and inclusions in olivine

In lherzolites and harzburgites, olivine hosts dendritic intragranular thin microveins (1–5 μm in thickness) consisting of colourless and transparent silicate glass, along with subordinate prismatic or rounded carbonates (1 – 5 μm in size; Fig. 4a, b, c). Associated with these microveins, olivine porphyroclasts preserve Type I fluid-rich melt inclusions (1 – 10 μm), typically extending from the glassy microstructures (Fig. 4a, b, c). These multiphase inclusions contain variable proportions of CO_2-rich fluid (30–90 vol.%), quenched glass and daughter mineral phases (Fig. 4a–e). Raman spectroscopy identifies a CO_2-rich fluid component (73–99 mol.%) with high and variable N_2 (1 – 23 mol.%; Fig. 5a and inset) and, rarely, minor CO (<1 – 6 mol.% in harzburgites and < 2 mol.% in lherzolites). Mineral phases are identified by Raman analysis (e.g., Frezzotti et al., 2012) as Cr-spinel, Mg-calcite, pyrite, molybdenite and rare clinopyroxene and graphite (Fig. 5a, b, c, d).

In Type I microveins and inclusions, the silicate glass Raman spectra show bands at 490 and 970 cm^{-1}, consistent with alkaline glass, trachytic or phonolitic in composition (Fig. 5b; Frezzotti et al., 2012). Two EMPA analyses (Table 2) in inclusions (GL_{INC}) give phonolitic and rhyolitic compositions (Fig. 6) with high SiO_2, Al_2O_3, Na_2O, K_2O and TiO_2 (57.48 – 69.62 wt.%, 14.89 – 21.01 wt.%, 5.21 – 9.03 wt.%; 7.14 – 7.94 wt.%; 0.26 – 1.71 wt.%, respectively; all values given on a volatile-free basis) and low CaO, MgO and FeO (0.13

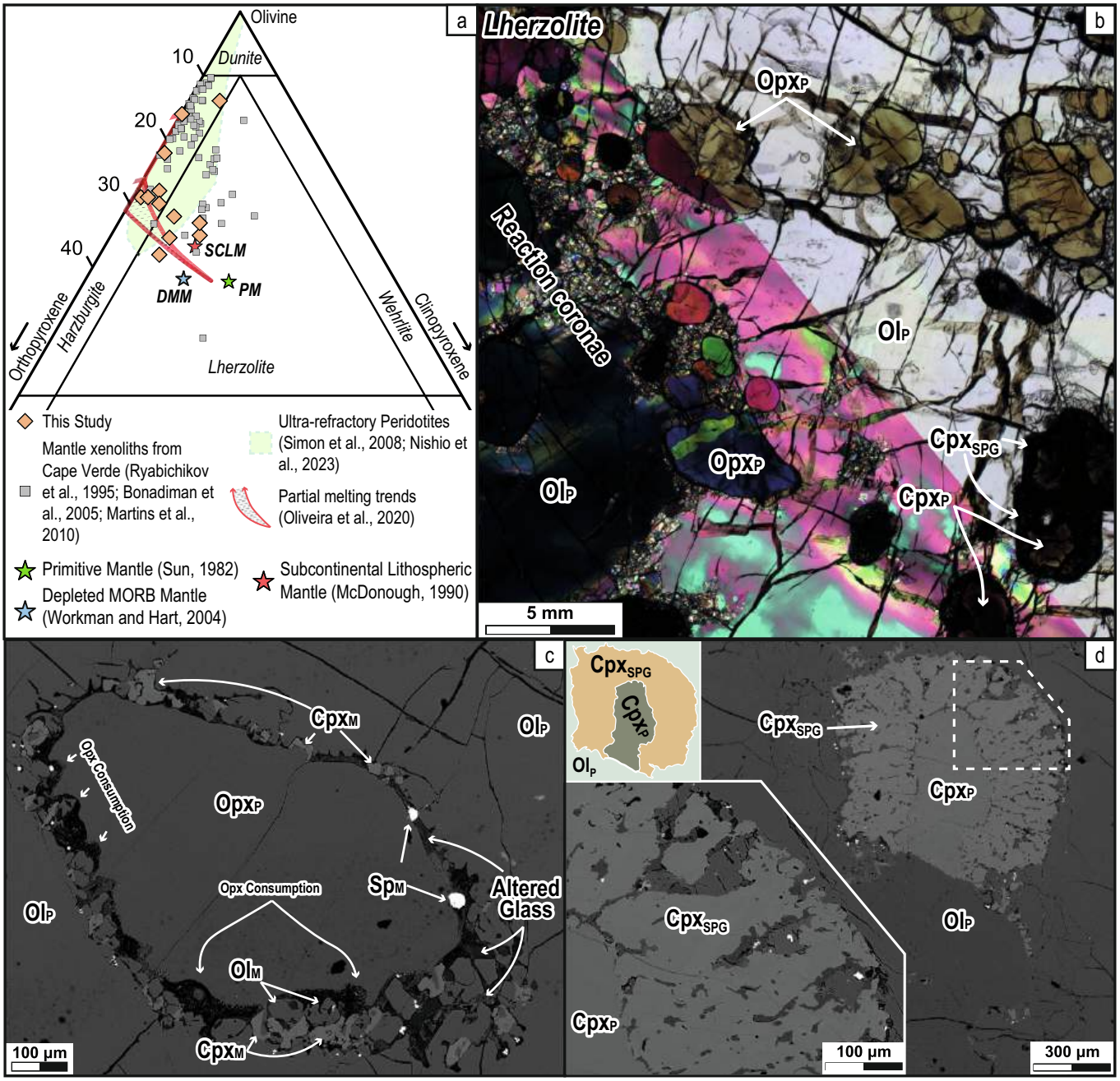

Fig. 2. (a) Classification diagram showing the studied mantle xenoliths and the literature data from Cape Verde. Reference mantle compositions are from Sun (1982), McDonough (1990), Workman and Hart (2004), Simon et al. (2008) and Nishio et al. (2023). Melting trends are from Oliveira et al. (2020) and Cape Verde published mantle xenoliths data are from Ryabchikov et al. (1995) and Bonadiman et al. (2005). SCLM stands for Subcontinental Lithospheric Mantle; DMM stands for Depleted Morb Mantle; PM stands for Primitive Mantle. Ol stands for olivine; Opx stands for orthopyroxene; Cpx stands for clinopyroxene; Sp stands for spinel. (b) Combined crossed and parallel polarisers photomicrographs displaying the characteristic poikilitic texture of lherzolites where large centimetric Ol_P oikocrysts include Cpx_P and Opx_P. The typical metasomatic reaction zone in lherzolites is also visible. (c) BSE image of corroded and Opx_P in lherzolites, surrounded by a thin reaction corona, in SAL1X. (d) BSE image of Cpx_{SPG} rims typically appear around a preserved Cpx_P core and corresponding sketch in the inset.

– 0.44 wt.%; 0.62 – 1.3 wt.%; 0.97 – 1.25 wt.%, respectively). The glass is peralkaline (AI = 1.09 – 1.12; Fig. 6c; Table 4) with Cl content up to 4600 ppm and totals of 94.7% – 99.3% (Table 2). These totals, combined with broad OH stretching features in the Raman spectra of glass (not shown), suggest H_2O contents in the range of units wt.%.

In glass, prismatic carbonates are identified as Mg-calcite and calcite (Raman bands at 1088, 715, 286, and 159 cm^{-1}, and 1086, 713, 279, and 152 cm^{-1}, respectively). In some samples (e.g., SAL1G), aragonite is also identified (Raman bands at 1086, 712, 708, 208, 181, 155, and 145 cm^{-1}, respectively; Fig. 5d, f). Rounded carbonates display broad and weak Raman bands at 1097 and 1088 cm^{-1}, corresponding to the fundamental ν_1 modes of dolomite and Mg-calcite, respectively (Fig. 5d, f). The broad and weak nature of these bands (FWHM 12 – 16 cm^{-1}) and the relative broadness and weakness, or absence, of the other significant ν_2, ν_3 and ν_4 bands indicates a high degree of crystallographic disorder and intergrowth at the (sub) micrometre scale (Fig. 5d and inset). Since Ca-Mg carbonate melt does not quench a glass, we interpret these aggregates as likely quench products of carbonate

Table 1
Mineral modal proportions of rock-forming minerals in Sal peridotitic xenoliths.

Sample	Olivine	Orthopyroxene	Clinopyroxene	Spinel	Lithology
Sal1S	71	28	1	0.1	Hzb
Sal3H	75	21	1	3.4	Hzb
Sal2C	70	26	4	0.1	Hzb
Sal3A	71	27	2	0.1	Hzb
SAL3F	72	25	3	0.1	Hzb
Sal1G	84	16	0.1	0.1	Hzb
SAL3D	86	10	4	0.5	Hzb
Sal1E	62	30	8	0.1	Lhz
Sal1A	65	27	8	0.1	Lhz
Sal1X	67	22	11	0.1	Lhz
Sal1F	66	22	12	0.1	Lhz
SAL3G	68	25	7	0.1	Lhz

melts. EPMA data (Table 3) indicate variable content of MgO (0.34 – 10.2 wt.%), FeO (0.48 – 4.22 wt.%) and SiO_2 (0.24 – 8.13 wt.%). Na_2O concentrations exceed K_2O (Na_2O: < 0.01 – 2.23 wt.%; K_2O: < 0.01 – 0.10 wt.%). High Cl (up to 2910 ppm) and S (SO_3 up to 3740 ppm) are present; in one analysis, the F content is 2640 ppm.

5.2. Type II – silicate glass – clinopyroxene – apatite + CO_2–(CO) fluids in relic orthopyroxene

A second population of fluid-rich melt inclusions (Type II) are restricted to relic Opx, which occurs as small clusters (up to 0.2 mm in diameter) and short intragranular trails (up to ~ 4 mm in length) extending from grain boundaries where coronae of Cpx_M + Ol_M + Spl_M + interstitial GL_M develop (Figs. 3b and 4f). Type II inclusions (1 – 25 μm in size) contain CO_2-rich fluid and silicate glass in highly variable proportions, suggesting heterogeneous trapping of a fluid-saturated melt (Frezzotti, 2001; Esposito, 2021). Daughter minerals in the glass (Fig. 4f–i) include phosphates, clinopyroxene, olivine, and Cr-spinel; carbonates are noticeably absent. Trails of CO_2-rich fluid inclusions (size 2 – 30 μm) also occur in the same Opx domains, often showing decrepitation textures (Viti and Frezzotti, 2001).

The glass in Type II inclusions shows Raman features that are similar to those of Type I inclusions in olivine (bands at 450 and 970 cm^{-1}; Fig. 5e). EMPA analyses (Table 2) show that, compared to Type I, Type II glass is dominantly trachytic, enriched in K_2O (4.13 – 12.28 wt.%; Fig. 6), depleted in TiO_2 and Na_2O (0.26 – 0.44 wt.%; 0.96 – 7.09 wt.%, respectively), and peraluminous (ASI 0.98 – 1.32; AI 0.67 – 0.92; Fig. 6c). Cl is up to 1200 ppm, and totals range from 89.0 wt.% to 100 wt.%.

Phosphates are dominated by Cl-rich apatite, identified by Raman bands at 962, 603, 591, 579, and 431 cm^{-1}. The ν_1 apatite mode is downshifted from 966 to 961 cm^{-1} with broad peaks (FWHM = 13 – 16 cm^{-1}), indicative of low F/Cl ratios (<0.3; Fig. 5e). Additional phosphates are tentatively identified based on their fundamental vibrations as whitlockite ($Ca_9Mg(PO_3OH)(PO_4)_6$, doublet at 975 and 960 cm^{-1}; Ionov et al., 2006) and brianite ($Na_2CaMg(PO_4)_2$; 985, 604, 586, 570, 1130, 1175 cm^{-1}; Ionov et al., 2006; Litasov and Podgornykh, 2017; Fig. 5e). Raman analysis also identified rare chalcopyrite. In harzburgites, Type II inclusions fluid phase consists of CO_2 with 1 – 17 mol.% CO (Fig. 5a), while in lherzolites it is nearly pure CO_2. N_2 is absent. Rare highly crystalline graphite is identified (Fig. 5a), and CO_2–CO mixtures occasionally show amorphous carbon formation during laser heating, indicating metastability under analysis conditions.

6. Mineral chemistry

Selected samples have been analysed for in situ mineral and glass major elements composition. Average compositions are reported in Tables 4 and 5, and corresponding chemical variation diagrams for minerals are presented in Fig. 7. The complete dataset is available in Supplementary Data Table S1.

6.1. Harzburgites

In harzburgites, Ol_P has averages Mg# (=Mg/[Mg + Fe^{2+}]% molar) per sample (here onward, unless differently specified, compositional data are given as ranges of averages, with corresponding 1σ, in each sample) from 90.5 (±0.2) to 91.4 (±0.3), high NiO falls along the Mantle Array (averages around 0.36 ± 0.04 wt.% – 0.41 ± 0.04 wt.%; Takahashi, 1986; Fig. 7a), and CaO is low (averages around 0.01 ± 0.01 wt.% – 0.07 ± 0.05 wt.%; Fig. 7b). Opx_P is enstatite, showing a high Mg# from 91.3 ± 0.5 to 92.8 ± 0.7, generally low, although variable, Al_2O_3 (around 1.88 ± 0.09 wt.% – 4.21 ± 0.16 wt.%; Fig. 7c), and high Cr_2O_3 (0.43 ± 0.06 wt.% – 0.83 ± 0.01 wt.%) and CaO (0.68 ± 0.11 wt.% – 1.39 ± 0.58 wt.%). In five samples (Sal3H, SAL1S, SAL3F, SAL2C, SAL3A), Cpx_P is diopside (X_{WO} = 0.46 ± 0.02 – 0.48 ± 0.02; Fig. 7d), with negligible aegirine component ($NaFe^{3+}Si_2O_6$; $X_{AEG} \ll 0.01$). Cpx_P is characterised by high Mg# from 93.4 ± 0.3 to 93.9 ± 0.3, and variable Cr_2O_3 (0.84 ± 0.12 wt.% – 0.92 ± 0.07 wt.%), while Al_2O_3, Na_2O, and TiO_2 are low (1.93 ± 0.25 wt.% – 2.46 ± 0.12 wt.%, 0.04 ± 0.03 wt.% – 0.16 ± 0.03 wt.% and 0.01 ± 0.02 wt.% – 0.08 ± 0.03 wt.%, respectively; Fig. 7e, f, g). In two harzburgites, which show the highest Ol contents (Ol: 84 – 86 vol.%, SAL1G and SAL3D; Table 1), Cpx is Mg-augite to diopside (X_{WO}: 0.42 ± 0.01 – 0.45 ± 0.00; Fig. 7d) with a higher aegirinic component (X_{AEG} = 0.04). Mg-augite has relatively low Mg#, ranging from 90.1 ± 0.3 to 91.4 ± 0.9, while TiO_2 and Na_2O are high (averages around 0.15 ± 0.02 wt.% – 0.17 ± 0.17 wt.% and 0.95 ± 0.14 wt.% – 1.10 ± 0.68 wt.%, respectively; Fig. 7f, g).

Rare Sp_P is Cr-spinel and has low Mg# (averages around 68.7 ± 2.7 – 72.1 ± 1.0) and high Cr# (averages around 45.1 ± 0.0 – 51.2 ± 0.1; Cr#=Cr/[Cr + Al]% molar; Fig. 7h). In sample SAL3D, Sp_P has the highest Mg# (average around 79.5 ± 1.7) and the lowest Cr# content (16.2 ± 0.5; Fig. 7h). Spongy rims (Sp_{SPG}) around Sp_P in harzburgites have a wide and scattered compositional range, characterised by lower Mg# (ranging from 50.6 to 76.1) and much higher Cr# contents (from 46.4 to 96.2).

6.2. Lherzolites

Lherzolite mineral chemistry is consistent with previous studies (Bonadiman et al., 2005, 2011; Shaw et al., 2006). In lherzolites, Ol has high Mg# ranging from 89.0 ± 0.1 to 90.4 ± 0.1, close to that of harzburgites SAL3D and SAL1G. NiO content falls within the Olivine Mantle Array (averages around 0.31 ± 0.07 wt.% – 0.37 ± 0.04 wt.%; Fig. 7a; Takahashi, 1986), and CaO is low (averages around 0.15 ± 0.01 wt.% – 0.18 ± 0.02 wt.%; Fig. 7b). Porphyroclastic Opx is enstatite, and has Mg# from 89.6 ± 0.4 to 90.9 ± 0.5, high Al_2O_3 (5.

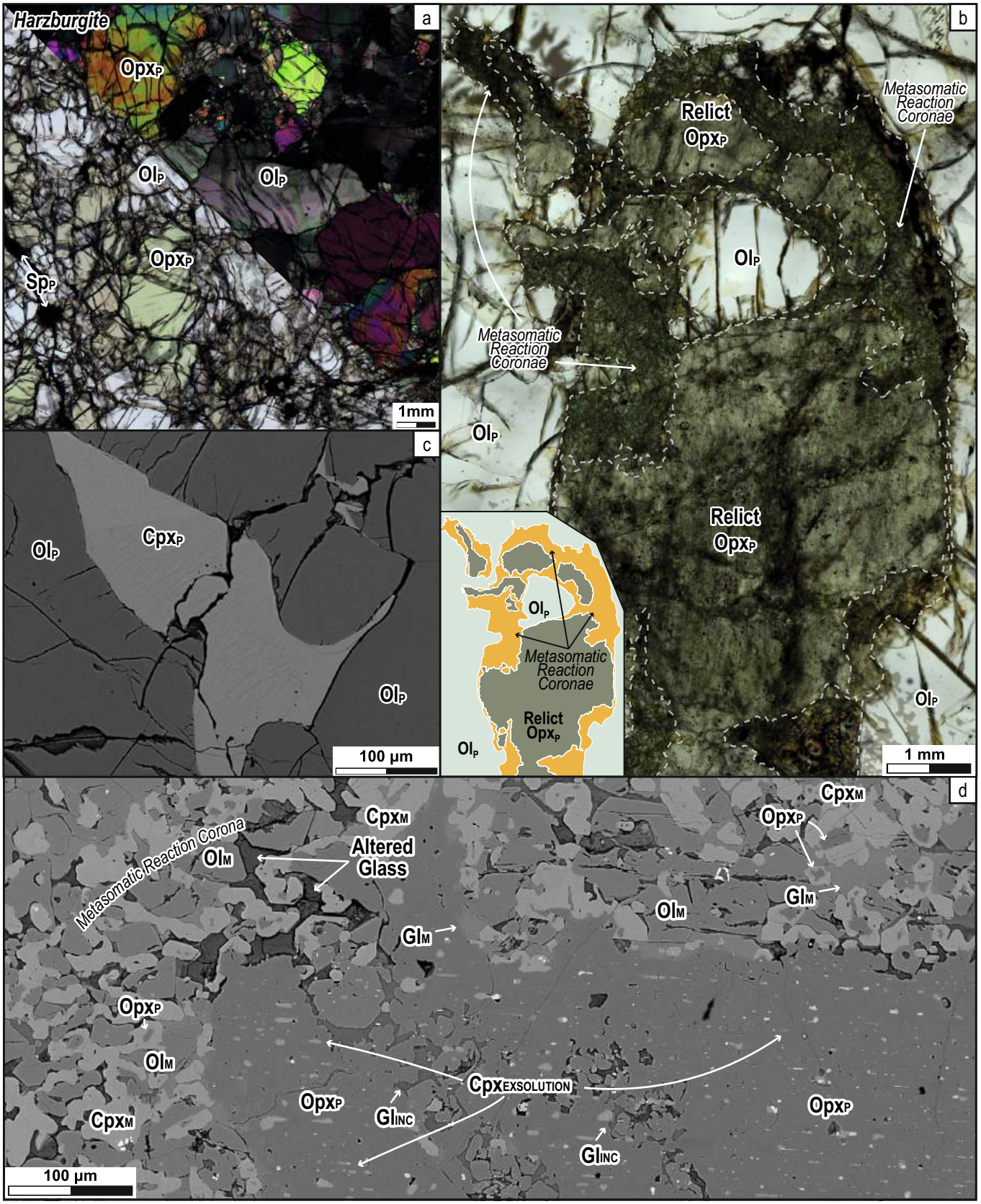

Fig. 3. (a) Combined crossed and parallel polarisers photomicrographs displaying the typical protogranular texture of harzburgites. (b) Corroded and relic Opx_P in harzburgites, surrounded by a thick reaction corona in SAL1G. The photo was obtained using a convergent lens. The inset contains a microstructural sketch clarifying the extent of the reaction corona. (c) BSE image of typical interstitial Cpx_P with exsolution lamellae of Opx at the core. (d) BSE images of a microgranular reaction zone around Opx_P in harzburgites where Cpx_M, Ol_M and an interstitial glass (but also the altered one) are visible and show the overgrowth and the corrosion of Cpx_M over Opx_P. Mineral abbreviations as in Fig. 2.

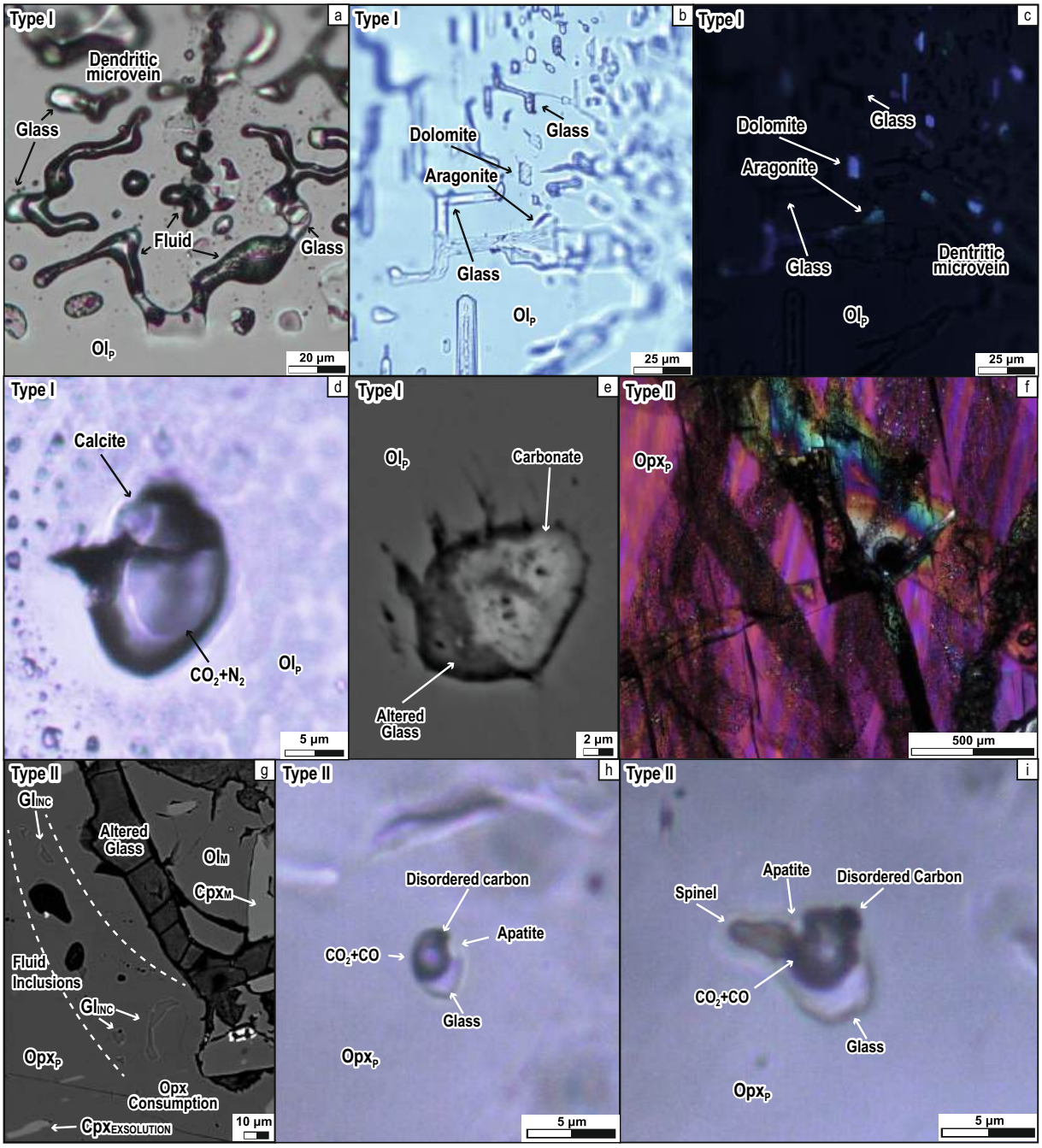

Fig. 4. (a) Typical dendritic glassy + fluid microvein in Ol_P. (b, c) Dendritic glassy + carbonate trail with aragonite and dolomite crystals. (d) Photomicrograph of a Type I inclusion containing carbonate and a fluid mixture of CO_2 and N_2. (e) Photomicrograph of Opx_P where multiple melt and fluid inclusions trails with birefringent solids depart from a metasomatic domain. (f) The BSE image shows fluid (empty voids) and melt inclusions without crystals, representing examples of GL_{INC} in Opx_P in contact with a metasomatic reaction coronae. On the right is visible the typical appearance of altered GL_M. (g, h) Photomicrographs of Type II inclusions containing in varying proportions silicate glass, apatite, spinel, disordered carbon, and a fluid mixture of CO_2 and CO. (i) BSE image of a carbonate within a Type II melt inclusion in which the glass has been altered. Mineral abbreviations as in Fig. 2.

25 ± 0.09 wt.% – 5.38 ± 0.06 wt.%), Cr_2O_3 (0.92 ± 0.05 wt.% – 0.95 ± 0.04 wt.%) and CaO contents (1.61 ± 0.04 wt.% – 1.76 ± 0.03 wt.%; Fig. 7c; Table 4). Cpx is Mg-augite in composition (X_{WO}: 0.35 ± 0.00 – 0.37 ± 0.01; Fig. 7d) with an appreciable aegirine component (X_{AEG} = 0.04). Cpx has a substantially lower Mg# (87.7 ± 0.2 – 89.0 ± 0.4) than Ol and Opx. It has high Al_2O_3 (6.19 ± 0.18 wt.% – 6.27 ± 0.13 wt.%; Fig. 4e), Cr_2O_3 (1.29 ± 0.06 wt.% – 1.46 ± 0.05 wt.%), Na_2O (1.01 ± 0.07 wt.% – 1.16 ± 0.07 wt.%; Fig. 7f), and TiO_2 (0.57 ± 0.08 wt.% – 0.65 ± 0.04 wt.%; Fig. 7g). Spongy rims in Cpx (Cpx_{SPG}) are Mg-augite with a negligible aegirinic component (X_{AEG} < 0.02) (Fig. 7d). Relatively to cores, they show an increase of Mg# (from 88.6 ± 0.2 to 90.2 ± 0.3) and Cr_2O_3 (1.38 ± 0.12 wt.% – 1.56 ± 0.11 wt.%), and a decrease of Al_2O_3 (4.37 ± 0.53 wt.% – 4.61 ± 1.05 wt.%; Fig. 7e), Na_2O (0.36 ± 0.10 wt.% – 0.40 ± 0.05 wt.%) and TiO_2 (averages around 0.58 ± 0.13 wt.% – 0.67 ± 0.09 wt.%). These data suggest a depletion in fusible components, indicating that spongy rims in Cpx are derived from partial melting during xenolith heating on ascent in the host lava (e.g., Shaw et al., 2006; Bonadiman et al., 2011). In SAL3G, the composition of Opx_P (higher Mg# and Cr_2O_3 and poorer in Al_2O_3 than Opx_P in other

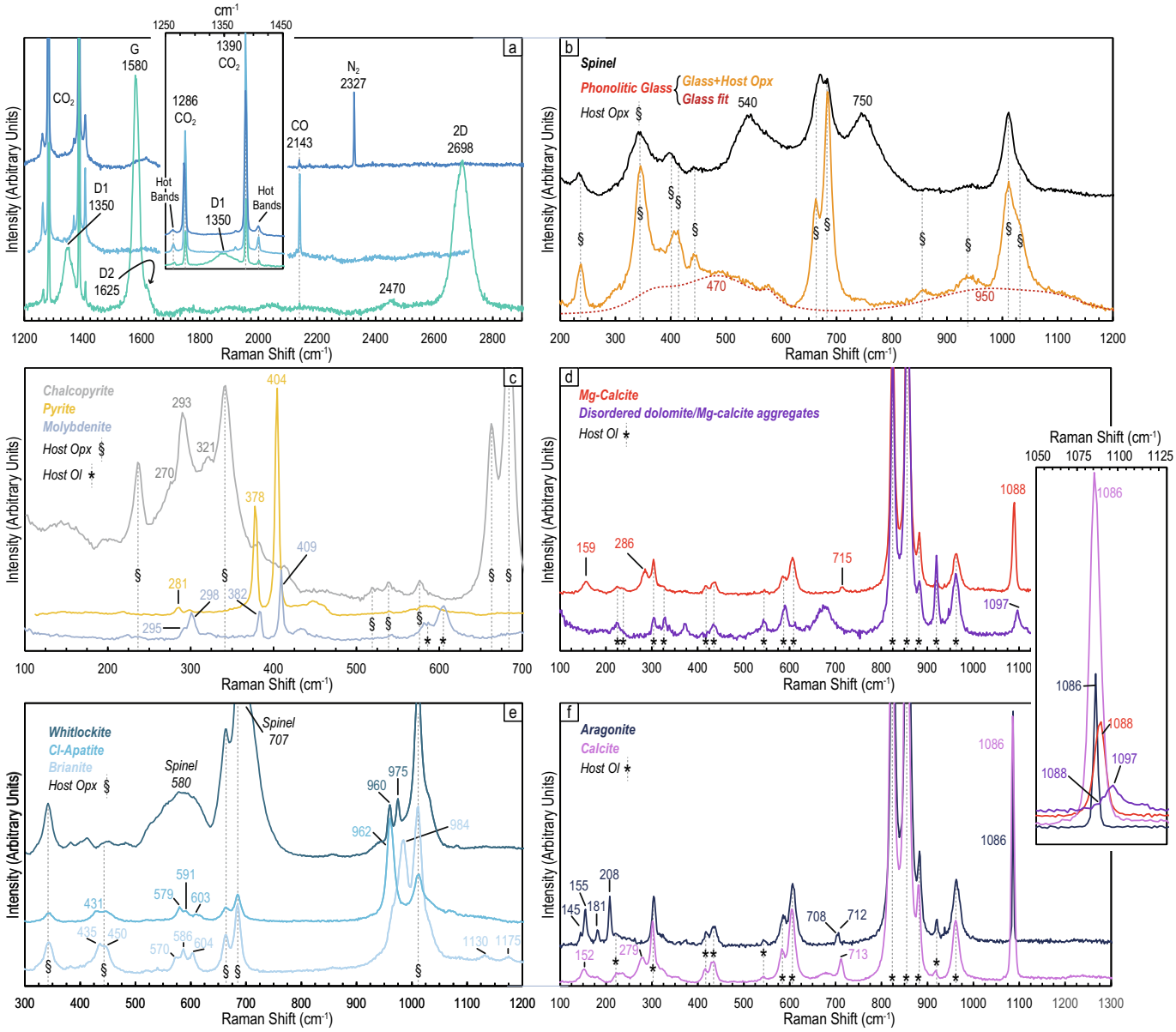

Fig. 5. Representative Raman spectra of minerals, glass and fluid phases found in the analysed fluid and melt inclusions. Vibrations marked with a dotted line and an asterisk "*" are the vibrations of the host olivine. In contrast, vibrations marked by a dotted line and the symbol "§" identify vibrations from the host orthopyroxene. Mineral abbreviations are as in Fig. 2.

harzburgites), coupled with the lack of preserved Cpx_P, now fully substituted by Cpx_{SPG}, suggest that this sample has been intensely affected during entrainment in the host lava. Sp_P is Al-spinel with Mg# (71.9 ± 0.0 – 76.2 ± 1.6) and Cr# (averages around 25.7 ± 0.0 – 26.3 ± 0.6). Spongy rims (Sp_{SPG}) around Sp_P, like in harzburgites, have a broad and scattered compositional range with lower Mg# (ranging from 66.6 to 78.4) and higher Cr# (ranging from 18.9 to 74.3).

6.3. Metasomatic coronae and microveins

Mineral phases in coronae and microveins show similar compositions in harzburgites and lherzolites. Ol_M Mg# ranges from 89.1 ± 0.3 to 91.9 ± 0.3, similar to or slightly higher than primary Ol porphyroclasts in lherzolites and harzburgites. NiO is considerably lower (0.18 ± 0.03 wt.% – 0.27 ± 0.00 wt.%; Fig. 7a; Table 5), and CaO is higher (0.12 ± 0.01 wt.% – 0.20 ± 0.04 wt.%; Fig. 7b). Metasomatic Cpx_M is Mg-augite to diopside (X_{WO} = 0.38 ± 0.01 – 0.45 ± 0.02; Fig. 7d), with a high aegirinic component (X_{AEG} = 0.01 0.06). Cpx_M has high Mg# (averages 91.6 ± 0.6 to 94.3 ± 0.3), and high and variable Na_2O and Cr_2O_3 (0.38 ± 0.04 wt.% – 1.52 ± 0.23 wt.%; 0.78 ± 0.28 wt.% – 3.33 ± 0.79 wt.%; Fig. 7f). Al_2O_3 and TiO_2 are low (0.15 ± 0.02 wt.% – 1.87 ± 0.43 wt.%, and 0.05 ± 0.05 wt. % – 0.58 ± 0.07 wt.%, respectively; Fig. 7e, g). Clinopyroxene in microveins and coronae around Opx is similar to "primary" Mg-augite in two harzburgites (SAL1G and SAL3D), although with higher Mg#. At the same time, it differs considerably in composition from Mg-augite in lherzolites (Fig. 7e–g). Euhedral Spl_M (Fig. 7h) are Cr-spinel, with variable composition Mg# (ranging from 70.2 to 78.8) and Cr# (ranging from 30.4 to 53.1).

In both harzburgites and lherzolites, interstitial glass in coronae (Gl_M; Figs. 2c and 3d; Fig. 6) has high SiO_2, Al_2O_3 and K_2O (64.5 – 67.6 wt.%, 13.4 – 17.3 wt.%, 15.7 – 17.2 wt.%, respectively; all values given on a volatile-free basis; Fig. 6; Table 2). Na_2O, CaO, and

Table 2
Average major element compositions (wt.%) of primary olivine, orthopyroxene, clinopyroxene and spinel in each analysed sample. The complete dataset can be found in Supplementary Data Table S1.

Sample	SAL1G	SAL3A	SAL1G	SAL1G	SAL1G	SAL1G	SAL1G	SAL1G	SAL1G	SAL2C	SAL2C	SAL1X
Analysis #	2	6	4	BIS-1	6	BIS-22	BIS-4	S60-16	S65-23	S15-8	S25-18	S50-3
Lithology	Hzb	Hzb	Hzb	Hzb	Hzb	Hzb	Hzb	Hzb	Hzb	Hzb	Hzb	Lhz
Microstructural Position	GL_{INC} in Ol	GL_{INC} in Ol	GL_{INC} in Opx	GL_{INC} in Opx	GL_{INC} in Opx	GL_{INC} in Opx	GL_{INC} in Opx	GL_M	GL_M	GL_M	GL_M	GL_M
SiO_2	57.09	65.86	60.52	53.14	58.49	64.28	66.61	64.11	66.1	66.16	64.55	63.72
TiO_2	1.7	0.15	0.26	0.27	0.27	0.42	0.39	0.09	0.18	0.1	0.09	0.18
Cr_2O_3	0	0.09	0.05	0.07	0.08	0.06	0	0	0.02	0.03	0.03	0.01
Al_2O_3	20.87	14.09	23.34	17.34	22.1	15.38	16.34	14.6	13.61	13.89	14.82	17.06
FeO	1.1	1.34	2.44	1.31	2.25	1.49	1.29	0.66	0.72	0.63	0.6	0.6
MnO	0.02	0.02	0.02	0	0.01	0.01	0.03	0.02	0.03	0.02	0	0.03
MgO	0.62	1.26	0.41	3.17	0.78	2.67	2.44	0.17	0.21	0.37	0.44	0.89
CaO	0.44	0.13	0.31	1.04	0.31	0.21	0.21	0	0	0.06	0.03	0.28
Na_2O	8.97	4.93	7.06	4.11	6.29	0.93	1.08	0.8	0.78	0.98	1.21	0.42
K_2O	7.89	6.75	5.12	8.43	4.13	11.37	12.28	16.67	16.09	16.11	15. 98	15.48
Cl	0.46	0.05	0.09	0.12	0.1	0.12	0.1	0	0.01	0.01	0.03	0.08
SO_3	0.06	0	0.03	0	0.05	0	0	0.02	0	0	0	0.01
F	0.09	0	0	0	0	0	0	0	0	0.02	0	0
Total	99.3	94.67	99.64	89	94.85	96.93	100.76	97.15	97.81	98.38	97.78	98.75
Alumina Saturation Index	0.87	0.9	1.32	0.98	1.44	1.08	1.06	0.75	0.73	0.73	0.77	0.95
Alkalinity Index	1.12	1.09	0.74	0.92	0.67	0.9	0.92	1.33	1.37	1.37	1.3	1.02

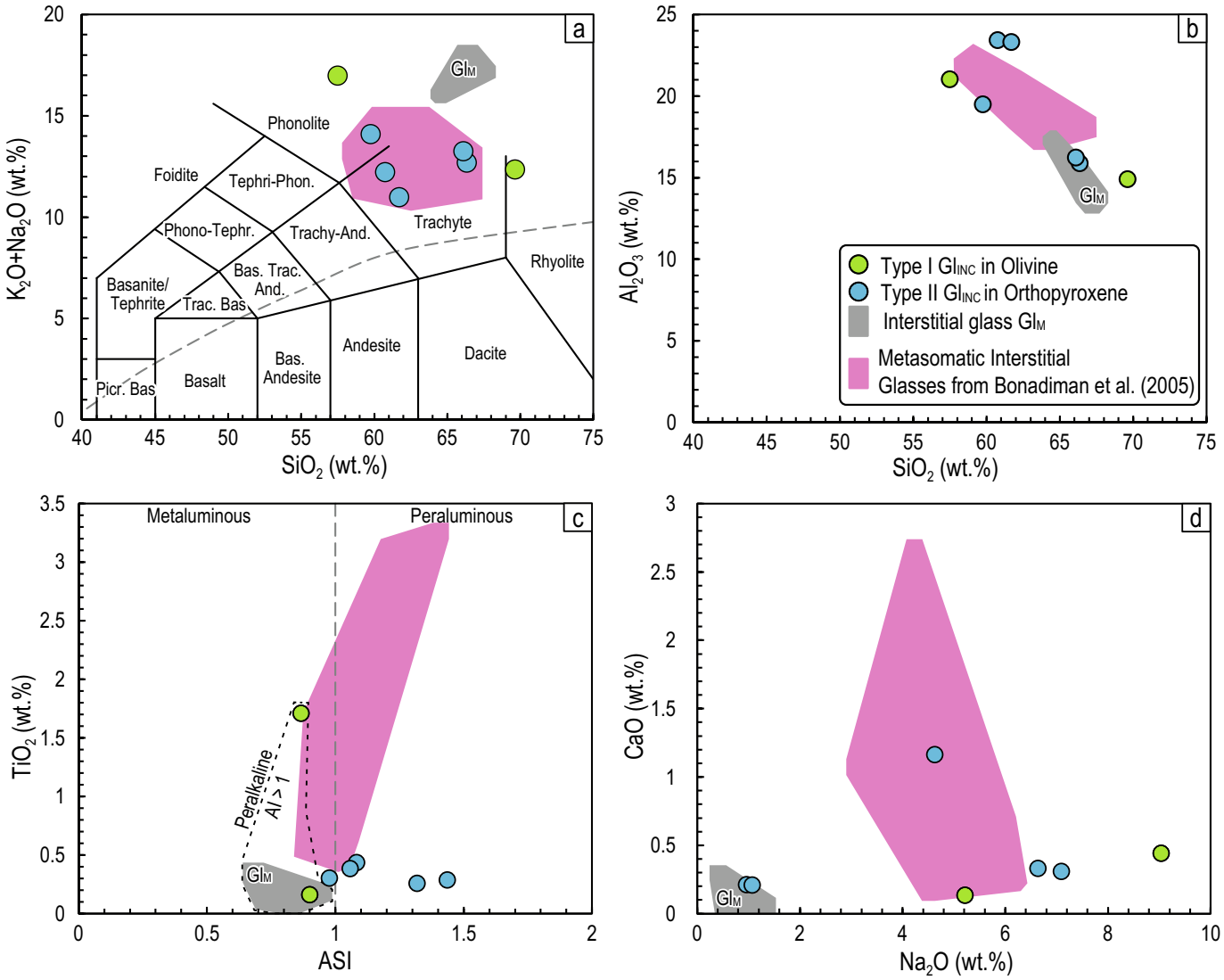

Fig. 6. Glass geochemistry. Total Alkali vs Silica plot from Le Maitre et al. (2002). Data plotted on a volatile-free basis. ASI stands for Allumina Saturation Index.

Table 3
Average major element compositions (wt.%) of metasomatic and secondary olivine, clinopyroxene and spinel in each analysed sample. The complete dataset can be found in Supplementary Data Table S1.

Sample	SAL3A	SAL3A	SAL3A	SAL3A	SAL3A	SAL3A	SAL3A
Analysis #	12	15	16	21	24	25	11
Lithology	Hzb	Hzb	Hzb	Hzb	Hzb	Hzb	Hzb
SiO_2	5.39	8.13	3.94	6.71	0.24	5.79	2
TiO_2	0.05	0.08	0.05	0.04	0.01	0.02	0
Cr_2O_3	0.07	0	0	0.01	0.01	0.02	0.03
Al_2O_3	0.07	0.14	0.06	0.02	0.01	0.01	0.03
FeO	2.15	4.22	1.54	0.72	0.48	0.51	1.16
MnO	0.05	0.03	0.07	0.01	0	0	0.12
MgO	4.51	10.12	2.88	2.47	0.35	0.88	4.67
CaO	49.53	40.94	51.96	51.74	54.37	47.49	41.2
Na_2O	0.1	0.03	0	0.01	0.05	0.15	2.23
K_2O	0.01	0	0	0	0.01	0	0.1
Cl	0.04	0.29	0.07	0.01	0	0.01	0.05
SO_3	0.04	0.03	0.05	0	0	0.02	0.37
F	0	0	0	0	0	0	0.26
Total	62.01	64.02	60.62	61.74	55.52	54.9	52.24
Mg#	78.9	81.04	76.92	85.91	56.02	75.27	87.72

TiO_2 content are low (0.4 – 1.3 wt.% and < 0.01 – 0.28 wt.%, and 0.05 – 0.34 wt.%, respectively). GL_M is peralkaline (Allumina Saturation Index, ASI = 0.68 – 0.95; Alkalinity Index, AI = 1.02 – 1.47; Fig. 6c). GL_M glass has little to no Cl (<0.08 wt.%) and a total of 95.2 wt.% and 99.7 wt.%.

6.4. Trace elements

We analysed Cpx and Opx in four harzburgites (SAL3H, SAL2C, SAL1S, SAL3D) and in three lherzolites (SAL1F, SAL1X, SAL1E) for in-situ trace elements by LA-ICPMS, with the aim of retrieving the melting degree of the mantle below Sal and identifying any eventual metasomatic enrichments in the primary minerals. Metasomatic minerals and glasses were not analysed because they were too small to avoid contamination from the host or surrounding phases. Trace element compositions of minerals have been reported in Supplementary Data Table S1, and corresponding Primitive Mantle Normalised (PM-normalised) incompatible elements and Chondrite normalised (Ch-normalised) Rare Earth Elements (REE) patterns are reported in Fig. 8. Elements below the detection limit are not plotted in the relevant figures nor reported in Supplementary Data Table S1.

In harzburgites, the multi-element PM-normalised plot (Fig. 8a) of primary diopsidic Cpx incompatible trace elements shows a depleted pattern, with most analyses showing some Large Lithophile Elements (LILE) and High Field Strength Elements (HFSE) below the detection limit. Light REE (LREE) in Ch-normalised plot (Fig. 8b) are strongly depleted relative to Heavy REE (HREE) (e.g., La_N/Yb_N = 0.005 – 0.267), consistent with high degrees of melt extraction. However, in some samples, the presence of a bland, concave upward LREE pattern and positive Pb and Ti anomalies suggests incipient metasomatic refertilisation in harzburgites. Opx shows similarly steep REE depletion, with LREE and MREE mostly below the detection limit, consistent with high degrees of melt extraction from 20% to 40% relative to a primitive mantle composition (Fig. 8c).

Primary Mg-augite in one harzburgite sample (SAL3D) is enriched in LILE, such as Th, U, and LREE, while HFSE (Nb, Ta, Zr, Hf and Ti) show negative anomalies. In this sample, Mg-augite trace element fractionation patterns resemble those associated with carbonatitic metasomatism or silicate melt, on porous flow (Coltorti et al., 1999; Grégoire et al., 2000; Moine et al., 2004). Mg-augite has a convex REE pattern in Ch-normalised plots with a flat MREE-HREE slope (La_N/Yb_N = 4.67 – 7.43; Fig. 8a, b). In this sample, Opx_P in Sal3D shows a concave upward REE pattern: MREE and HREE record melt extraction between 5% and 15%, while LREE show slight enrichment, pointing to a metasomatic overprint (Fig. 8c). Conversely, primary Mg-augite in lherzolites show incompatible trace element enrichment with a convex-downward pattern (Fig. 8a). LILE and HFSE (except Ti) are depleted relative to REE. LREE enrichment relative to HREE in PM-normalised and Ch-normalised plots (La_N/Yb_N = 0.89 – 1.57; Fig. 8a, b). In Cl-normalised plots, Mg-augite Cpx_P is characterised by a convex pattern that reflects more fertile compositions than typical primitive mantle composition. Opx_P from lherzolites shows REE contents higher than primitive mantle compositions (Fig. 5c), although LREE are depleted relative to MREE and HREE.

7. Geothermobarometry

In lherzolites and harzburgites, we applied the Opx-Cpx Fe-Mg exchange thermometer by Brey and Köhler (1990), combined with the Ca-in-Ol barometer of Köhler and Brey (1990) and the empirical Ca-Mg#-in-Ol barometer of Shejwalkar and Coogan (2013). Calculations were performed iteratively using the compositions of the cores of primary olivine (Ol_P), orthopyroxene (Opx_P), clinopyroxene (Cpx_P), and the composition of metasomatic olivine (Ol_M), clinopyroxene (Cpx_M) and the rims of orthopyroxene in contact with the metasomatic domains. Results report uncertainties as the combination of the standard deviation of individual analyses and the intrinsic error of the thermobarometric equations. The complete dataset is reported in Supplementary Data Table S2.

The calculated temperatures show a bimodal distribution (Fig. 9a and b) that is outside the geothermometer intrinsic error. The first cluster is obtained from representative core compositions of Ol_P, Opx_P, and Cpx_P, as well as the composition of Cpx exsolution in Opx_P in five harzburgites (SAL3H, SAL1S, SAL2C, SAL3D, SAL1G), with temperatures ranging from 958 ± 15 °C to 1061 ± 27 °C, clustering around 1000 1025 °C. Notably, the least metasomatised samples, SAL1S and SAL3H, display the lowest temperatures at 958 ± 15 °C and 974 ± 50 °C, respectively. Conversely, sample SAL1G, which exhibits the most extensive textural evidence of metasomatic reactions, shows a higher temperature of approximately 100 °C, with a clustering at 1061 ± 27 °C. Thermometers were not applied to primary lherzolite mineral assemblages since Cpx_P composition is out of equilibrium with Opx_P ($Kd_{Mg\text{-}Fe}$ Opx-Cpx < 0.78). The second cluster of temperatures, calculated from mineral assemblages in metasomatic paragenesis in three harzburgites (SAL1G, SAL2C, SAL3H) and three lherzolites (SAL1E, SAL1X, SAL1F), ranges from 1140 ± 15 °C to 1200 ± 25 °C.

Table 4
Composition (wt.%) of included glass (GL_{INC}) and selected interstitial glasses inside metasomatic reaction coronae (GL_M). The complete dataset can be found in Supplementary Data Table S1.

Sample	SAL1S		SAL3H		SAL2C		SAL3A		SAL3F		SAL1G		SAL3D		SAL1E		SAL1F		SAL1X		SAL3G	
Lithology	Hzb		Hzb		Hzb		Hzb		Hzb		Hzb		Hzb		Lhz		Lhz		Lhz		Lhz	
Mineral	Ol_P		Ol_P		Ol_P		Ol_P		Ol_P		Ol_P		Ol_P		Ol_P		Ol_P		Ol_P		Ol_P	
n	8	σ	10	σ	4	σ	3	σ	5	σ	9	σ	5	σ	3	σ	5	σ	3	σ	4	σ
SiO_2	41.54	0.52	40.92	0.33	41.23	0.27	40.55	0.48	41.84	0.4	40.5	0.41	41.59	0.26	41.03	0.1	41.22	0.26	40.14	0.3	41.11	0.22
TiO_2	0.02	0.02	0.03	0.03	0.01	0.03	0.01	0.02	0	0	0.01	0.01	0.02	0.02	0.03	0.03	0.01	0.02	0.01	0.01	0.03	0.03
Al_2O_3	0.02	0.01	0.01	0.01	0	0.01	0.02	0.01	0.01	0.01	0.01	0.01	0.01	0.02	0.12	0.13	0.05	0.01	0.08	0.01	0.05	0.03
Cr_2O_3	0.02	0.03	0.02	0.03	0.02	0.03	0.03	0.02	0.02	0.02	0.03	0.03	0.02	0.02	0.05	0.05	0.06	0.02	0.1	0.03	0.13	0.05
FeO	8.81	0.12	8.51	0.5	8.24	0.32	8.78	0.06	8.77	0.17	9.29	0.28	9.38	0.23	9.38	0.14	9.66	0.09	10.64	0.15	8.84	0.2
MnO	0.15	0.03	0.13	0.03	0.14	0.02	0.13	0.03	0.12	0.02	0.17	0.05	0.12	0.03	0.14	0.02	0.14	0.04	0.15	0.02	0.11	0.03
NiO	0.4	0.03	0.36	0.04	0.39	0.04	0.34	0.04	0.41	0.04	0.35	0.05	0.38	0.03	0.31	0.07	0.35	0.04	0.37	0.04	0.4	0.06
MgO	51.14	0.23	50.5	1.05	49.27	0.12	50.9	0.26	50.92	0.24	49.45	1.07	50.31	0.4	49.39	0.23	48.93	0.74	48.14	0.32	50.2	0.27
CaO	0.01	0.01	0.02	0.03	0.05	0.06	0.07	0.05	0.04	0.02	0.06	0.02	0.06	0.04	0.16	0.01	0.15	0.01	0.18	0.02	0.16	0.02
Total	102.1	0.42	100.51	1.34	99.36	0.32	100.84	0.62	102.12	0.14	99.87	1.64	101.89	0.73	100.61	0.19	100.58	0.73	99.81	0.62	101.02	0.52
Forsterite	0.91	0	0.91	0.01	0.91	0	0.91	0	0.91	0	0.9	0	0.9	0	0.9	0	0.89	0	0.88	0	0.9	0
Fayalite	0.09	0	0.09	0	0.09	0	0.09	0	0.09	0	0.09	0	0.09	0	0.1	0	0.1	0	0.11	0	0.09	0
Mg#	91.19	0.11	91.36	0.51	91.42	0.29	91.18	0.02	91.18	0.14	90.46	0.23	90.53	0.18	90.37	0.14	90.03	0.15	88.97	0.07	91.01	0.17

Sample	SAL1S		SAL3H		SAL2C		SAL3A		SAL3F		SAL1G		SAL3D		SAL1E		SAL1F		SAL1X		SAL3G	
Lithology	Hzb		Hzb		Hzb		Hzb		Hzb		Hzb		Hzb		Lhz		Lhz		Lhz		Lhz	
Mineral	Opx_P		Opx_P		Opx_P		Opx_P		Opx_P		Opx_P		Opx_P +Opx_{EX}		Opx_P		Opx_P		Opx_P		Opx_P	
n	9	σ	18	σ	7	σ	6	σ	3	σ	11	σ	11	σ	20	σ	7	σ	6	σ	10	σ
SiO_2	57.59	0.62	56.64	0.34	56.72	0.31	56.19	0.31	57.47	0.53	56.36	0.6	56.6	0.22	53.96	0.24	54.47	0.29	53.01	0.26	54.94	0.39
TiO_2	0.02	0.02	0.01	0.01	0.02	0.02	0.01	0.02	0.02	0.01	0.04	0.03	0.05	0.02	0.26	0.04	0.29	0.04	0.29	0.02	0.26	0.04
Al_2O_3	2.24	0.15	2.08	0.28	2.2	0.13	1.88	0.09	2.34	0.03	2.47	0.44	4.21	0.16	5.36	0.14	5.25	0.09	5.38	0.06	3.9	0.12
Cr_2O_3	0.7	0.12	0.69	0.14	0.7	0.09	0.66	0.07	0.83	0.01	0.62	0.11	0.43	0.06	0.95	0.04	0.92	0.05	0.92	0.03	1.16	0.06
Fe_2O_3	0.16	0.46	0.64	0.57	0.35	0.33	0.99	0.55	0.14	0.25	1.01	0.58	0.31	0.45	0.46	0.36	0	0	0.41	0.27	0.38	0.4
FeO	5.57	0.47	4.82	0.47	4.97	0.3	4.77	0.52	5.57	0.26	4.94	0.68	5.75	0.4	5.66	0.37	6.1	0.13	6.38	0.26	5.17	0.39
MnO	0.15	0.04	0.13	0.03	0.14	0.03	0.15	0.03	0.12	0.02	0.16	0.03	0.13	0.02	0.13	0.03	0.14	0.03	0.15	0.03	0.11	0.04
NiO	0.11	0.05	0.09	0.04	0.11	0.04	0.09	0.04	0.12	0.06	0.09	0.04	0.08	0.08	0.11	0.04	0.1	0.04	0.09	0.06	0.14	0.02
MgO	34.17	0.4	34.27	0.72	33.84	0.63	34.27	0.46	34.15	0.18	34.23	0.51	33.91	0.23	31.59	0.29	31.01	0.28	30.65	0.07	32.4	0.21
CaO	1.39	0.58	1.08	0.23	1.35	0.42	1.21	0.57	1.29	0.36	0.81	0.31	0.68	0.11	1.6	0.04	1.61	0.03	1.76	0.03	1.69	0.03
Na_2O	0	0.01	0.01	0.02	0.01	0.02	0.03	0.03	0.03	0.03	0.15	0.26	0.03	0.03	0.13	0.06	0.15	0.01	0.1	0.06	0.17	0.06
Total	102.08	0.45	100.45	0.71	100.39	0.75	100.25	0.39	102.09	0.4	100.88	0.76	102.18	0.14	100.2	0.42	100.04	0.34	99.14	0.35	100.3	0.43
Wollastonite	0.03	0.01	0.02	0	0.03	0.01	0.02	0.01	0.02	0.01	0.02	0.01	0.01	0	0.03	0	0.03	0	0.04	0	0.03	0
Enstatite	0.89	0.01	0.9	0	0.89	0.01	0.89	0.01	0.89	0.01	0.89	0.01	0.89	0	0.87	0	0.86	0	0.85	0	0.88	0
Ferrosilite	0.09	0	0.08	0	0.08	0	0.08	0	0.09	0	0.09	0.01	0.09	0	0.1	0	0.1	0	0.11	0	0.09	0
Aegirine	0	0	0	0	0	0	0	0	0	0	0.01	0.01	0	0	0	0	0.01	0	0	0	0.01	0
Mg#	91.64	0.65	92.68	0.72	92.37	0.39	92.75	0.72	91.6	0.36	92.53	0.97	91.33	0.53	90.88	0.53	90.06	0.2	89.57	0.38	91.77	0.55

Sample	SAL1S		SAL3H		SAL2C		SAL3A		SAL1G		SAL3D		SAL1E		SAL1F		SAL1X	
Lithology	Hzb		Hzb		Hzb		Hzb		Hzb		Hzb		Lhz		Lhz		Lhz	
Mineral	Cpx_P		Cpx_P		Cpx_P		Cpx_P +Cpx_{Ex}		Cpx_P +Cpx_{Ex}		Cpx_P		Cpx_P		Cpx_P		Cpx_P	
n	9	σ	12	σ	3	σ	5	σ	7	σ	13	σ	9	σ	6	σ	6	σ
SiO_2	54.38	0.54	53.14	0.76	53.7	0.52	53.57	0.42	53.4	0.72	53.89	0.26	51.76	0.18	51.94	0.34	50.77	0.3
TiO_2	0.01	0.02	0.02	0.03	0.08	0.03	0.01	0.03	0.17	0.07	0.15	0.02	0.65	0.04	0.59	0.06	0.57	0.08
Al_2O_3	2.46	0.12	2.01	0.22	2.33	0.15	1.93	0.25	3.22	1.08	4.67	0.26	6.27	0.13	6.25	0.21	6.19	0.18
Cr_2O_3	0.92	0.07	0.84	0.12	0.92	0.06	0.86	0.08	1.45	0.41	0.66	0.08	1.44	0.05	1.46	0.05	1.29	0.06
Fe_2O_3	0	0	0	0	0	0	0	0	0	0	0	0	0	0	0	0	0	0
FeO	2.27	0.15	2.02	0.25	1.99	0.05	2.17	0.18	2.89	0.24	2.89	0.08	3.9	0.05	3.86	0.11	4.48	0.1
MnO	0.07	0.03	0.08	0.02	0.08	0.01	0.06	0.03	0.1	0.03	0.08	0.02	0.1	0.04	0.12	0.04	0.11	0.04
NiO	0.04	0.04	0.05	0.04	0.06	0.03	0.04	0.04	0.04	0.03	0.06	0.04	0.08	0.04	0.09	0.04	0.05	0.03
MgO	17.92	0.36	17.51	0.64	17.03	0.45	17.82	0.52	17.27	1.9	16.47	0.16	17.65	0.1	17.56	0.47	17.92	0.08
CaO	23.46	0.57	23.58	0.92	23.85	0.12	23.24	0.88	20.27	0.47	21.81	0.18	17.21	0.13	17.35	0.14	16.55	0.08
Na_2O	0.04	0.03	0.07	0.03	0.16	0.03	0.08	0.08	1.1	0.68	0.95	0.14	1.09	0.08	1.16	0.07	1.01	0.07
K_2O	0.01	0.01	0	0.01	0.01	0.01	0	0.01	0.01	0.01	0.01	0.01	0.01	0.01	0.01	0	0	0
Total	101.58	0.7	99.32	0.81	100.21	0.28	99.78	0.37	99.93	0.96	101.63	0.55	100.14	0.23	100.37	0.75	98.92	0.43
Wollastonite	0.47	0.01	0.48	0.02	0.48	0.01	0.46	0.02	0.42	0.01	0.45	0	0.37	0	0.37	0.01	0.35	0
Enstatite	0.5	0.01	0.49	0.02	0.48	0.01	0.5	0.02	0.49	0.04	0.47	0	0.52	0	0.52	0.01	0.53	0
Ferrosilite	0.04	0	0.03	0	0.03	0	0.04	0	0.05	0	0.05	0	0.07	0	0.07	0	0.08	0
Aegirine	0	0	0	0	0.01	0	0	0	0.04	0.03	0.04	0	0.04	0	0.04	0	0.04	0
Mg#	93.39	0.34	93.93	0.59	93.83	0.31	93.60	0.3	91.36	0.87	91.05	0.26	88.97	0.13	89.00	0.35	87.70	0.22

Sample	SAL1S		SAL3H		SAL2C		SAL3F		SAL3D		SAL1E		SAL1F		SAL1X	
Lithology	Hzb		Hzb		Hzb		Hzb		Hzb		Lhz		Lhz		Lhz	
Mineral	Spl_P		Spl_P		Spl_P		Spl_P		Spl_P		Spl_P		Spl_P		Spl_P	
n	1	σ	8	σ	2	σ	2	σ	8	σ	4	σ	4	σ	1	σ
SiO_2	0.03		0.02	0.01	0.01	0.01	0.02	0.01	0.05	0.02	0.19	0.02	0.18	0.02	0.12	
TiO_2	0		0.03	0.02	0.03	0.04	0.02	0	0.12	0.06	0.91	0.16	0.81	0.04	0.9	
Al_2O_3	32.98		28.25	0.75	27.85	0.17	27.87	0.09	54.28	1.86	44.77	1.49	43.71	1.69	42.69	
Cr_2O_3	40.38		43.8	0.61	42.58	0.28	43.56	0.06	15.58	0.34	23.17	0.32	23.25	0.09	22.04	
Fe_2O_3	0		1.21	0.73	1.6	1.01	1.91	0.08	1.34	1.64	1.78	2.06	3.17	2.03	3.31	
FeO	12.39		12.87	1.11	11.27	0.45	12.53	0.05	9.35	0.86	10.79	1.01	10.67	0.9	12.24	
MnO	0.06		0.09	0.03	0.04	0.06	0.11	0.01	0.08	0.04	0.06	0.03	0.07	0.03	0.06	
NiO	0.16		0.08	0.05	0.11	0.01	0.09	0.06	0.29	0.05	0.25	0.12	0.28	0.06	0.31	
MgO	16.13		15.83	0.77	16.34	0.43	15.96	0.02	20.33	0.53	19.17	0.64	19.13	0.42	17.56	
Total	102.13		102.17	0.23	99.81	0.49	102.05	0.16	101.46	1.59	101.13	0.26	101.26	0.9	99.23	
Mg#	69.89		68.65	2.72	72.09	0.95	69.41	0.08	79.49	1.72	75.99	1.97	76.18	1.59	71.89	
Cr#	45.09		51	0.87	50.63	0.01	51.19	0.08	16.16	0.48	25.78	0.55	26.32	0.6	25.72	

Table 5
Composition (wt.%) of carbonates associated with included glass inside opened melt inclusions.

Mineral	Spl_M		Spl_{SPG}		Spl_{SPG}		Spl_{SPG}		Spl_{SPG}		Spl_{SPG}		Spl_{SPG}		Spl_{SPG}	
n	6	σ	3	σ	2	σ	3	σ	1	σ	1	σ	3	σ	3	σ
SiO_2	0.14	0.04	0.19	0.32	0.03	0.04	0.05	0.02	0.16		0.18		0.16	0.11	0.11	0.06
TiO_2	0.35	0.16	0.08	0.1	0.01	0	0.75	1.03	0.64		0.11		1.53	0.57	1.1	0.46
Al_2O_3	31.03	6.85	25.74	7.58	29.04	0.09	13.39	8.6	1.78		47.32		21.61	11.29	42.78	7.77
Cr_2O_3	33.92	4.87	45.49	8.43	42.45	0.36	55.15	9.14	66.45		25.62		47.77	10.08	25.18	8.7
Fe_2O_3	7.19	2.6	1.35	1.02	2.7	0.38	4.59	2.24	2.29		0		0.23	0.2	2.55	1.89
FeO	10.79	0.94	14.44	1.24	10.39	0.61	14.07	3.33	17.26		9.66		13.5	1.88	11.24	1.84
MnO	0.1	0.06	0.09	0.06	0.08	0.01	0.07	0.07	0.25		0.07		0.09	0.07	0.1	0.03
NiO	0.2	0.07	0.11	0.03	0.06	0.08	0.1	0.06	0.06		0.09		0.06	0.06	0.24	0.1
MgO	17.37	1.39	14.7	1.18	17.56	0.37	13.92	2.32	9.9		19.29		15.28	2.36	18.95	1.5
Total	101.12	0.5	102.19	0.27	102.3	0.04	102.09	0.86	98.81		102.37		100.32	1.3	102.32	0.12
Mg#	74.07	2.84	64.41	3.12	75.06	1.05	63.67	7.51	50.55		78.07		66.62	5.16	74.98	3.73
Cr#	42.78	7.85	54.53	9.92	49.51	0.09	73.93	12.5	96.16		26.64		60.69	13.94	28.53	8.74

Pressure estimates span a broad range, with values from the same sample that are roughly inside the geobarometer intrinsic error, with slightly higher values in harzburgites (Fig. 9c and d). In three harzburgite samples (SAL1G, SAL3H, SAL1S), Cpx_P-Ol_P couples record the highest pressures between 3.5 ± 0.4 and 3.3 ± 0.6 GPa, or between 106 ± 13 and 103 ± 17 km, assuming a mantle density of 3.3 g/cm^3 and an overlying oceanic crustal thickness of 12 km, assuming a density of 2.9 g/cm^3 (rock densities from Winter (2014). Calculated depths agree with the finding in one harzburgite (SAL1G) of aragonite in metasomatic domains, which is stable at pressures > 2.7 – 3.3 GPa (i.e., roughly > 85 – 105 km, between 1000 and 1200 °C; Zhao et al., 2019). Metasomatic domains in samples SAL1G and SAL3H indicate near-isobaric conditions at 3.2 ± 0.4 GPa. Lower pressures are recorded for the primary assemblages and associated metasomatic domains of two harzburgite samples (SAL3D and SAL2C), from 2.6 ± 0.6 GPa (or 80 ± 17 km) to 2.2 ± 0.3 GPa (or 66 ± 9 km). In lherzolite samples (SAL1F, SAL1E, and SAL1X), the pressure estimates for metasomatic mineral assemblages range from 2.7 ± 0.4 GPa to 2.5 ± 0.4 GPa (or 83 ± 14 km to 76 ± 13 km depth).

8. Discussion

8.1. Nature of the lithosphere beneath Sal Island

The lithosphere beneath Sal Island is heterogeneous, consisting of spinel lherzolites and ultradepleted spinel harzburgites, as reported by several studies on Cape Verde mantle xenoliths (e.g., Bonadiman et al., 2005; Simon et al., 2008; Neumann and Simon, 2009; Coltorti et al., 2010). We also found that harzburgites indicate extensive melt extraction, as evidenced by a generally low modal abundance of clinopyroxene, which is typically less than 3 vol.%, and high Mg# in olivine, orthopyroxene, clinopyroxene, and spinel. The trace element pattern distribution in primary Cpx and Opx suggests at least 20% to 40% melt extraction in these rocks (Fig. 8).

Presented iteratively computed thermobarometric estimates (see Supplementary Material) indicate a thick lithosphere, consisting of fertile lherzolites and ultradepleted harzburgites sampled from ~ 66 to 83 km and of deeper harzburgitic roots down to about 106 km (Fig. 10). Independent evidence supporting high-pressure conditions for the origin of studied peridotites is provided by the presence of aragonite in Type I microveins in harzburgites, which is stable from pressures greater than 3.0 to 3.3 GPa (> 95 – 105 km; Zhao et al., 2019) at metasomatic temperatures around 1100 – 1200 °C (Fig. 10a). Notably, the calculated pressures in the deepest harzburgitic rocks fall at the transition between the spinel-garnet and spinel stability fields for a depleted harzburgitic mantle (Fig. 10a; see figure caption for computation details).

Calculated depths significantly exceed the typical lithosphere-asthenosphere boundary (LAB) beneath ocean islands, generally at less than 80 km depth (Rychert and Shearer, 2009; Schmerr, 2012). Mantle xenolith-derived depths align with seismic tomography studies, which image LAB depths from 90 to 125 km beneath the eastern islands of Cape Verde (Cazenave et al., 1988; Lodge and Helffrich, 2006; Vinnik et al., 2012; Lodhia et al., 2018; Liu and Zhao, 2021; Fig. 10b) and with predicted primitive magma generation depths of 110 – 150 km beneath Sal (Torres et al., 2010; Sun and Dasgupta, 2023; Villaseca et al., 2025). The relevant thickness and ultra-depleted nature of peridotites suggest that at least the roots of the mantle lithosphere beneath Sal Island could be subcontinental in origin, consistent with the style of magnetic anomalies observed in correspondence with the easternmost island of the archipelago (O'Reilly et al., 2009). Domains of ultrarefractory mantle have been previously identified at Cape Verde, interpreted as remnants of an ancient, cratonic, or subcontinental lithosphere (Fig. 11a; Bonadiman et al., 2005; Simon et al., 2008; Neumann and Simon, 2009; Coltorti et al., 2010). The chemical characteristics of some of the studied harzburgites, which plot along the Oceanic Mantle Melting Trend of Boyd (1980) coupled with Cr# in spinel are more akin to an off-craton composition rather than a cratonic one (Fig. 11b and c; Boyd, 1989; Pearson et al., 2003; Bernstein et al., 2006), in line with the presence of ancient thrust belts along the western margin of the West African Craton (Fig. 1a).

8.2. Metasomatic evolution

Previous studies of peridotites from Sal Island, particularly lherzolites, have documented widespread metasomatism by a kimberlite-type ultramafic melt, evolving toward SiO_2-saturated, K-rich mafic compositions (e.g., lamproite; Bonadiman et al., 2005). According to these authors, metasomatism observed in peridotites originating at depths from approximately 40 to 70 km is associated with the crystallisation of olivine, clinopyroxene, spinel, and K-feldspar, along with significant enrichment in REE. However, the metasomatic textures and chemical compositions of minerals and glass in deeper peridotites (from 66 to 106 km) from the current study suggest at least two main metasomatic events involving, respectively, alkali-rich silicate-carbonate melts and CO_2-rich silicate melts. Textural and compositional evidence for these metasomatic agents is preserved in both mineral assemblages and in inclusions and glass + carbonate microveins within olivine and orthopyroxene.

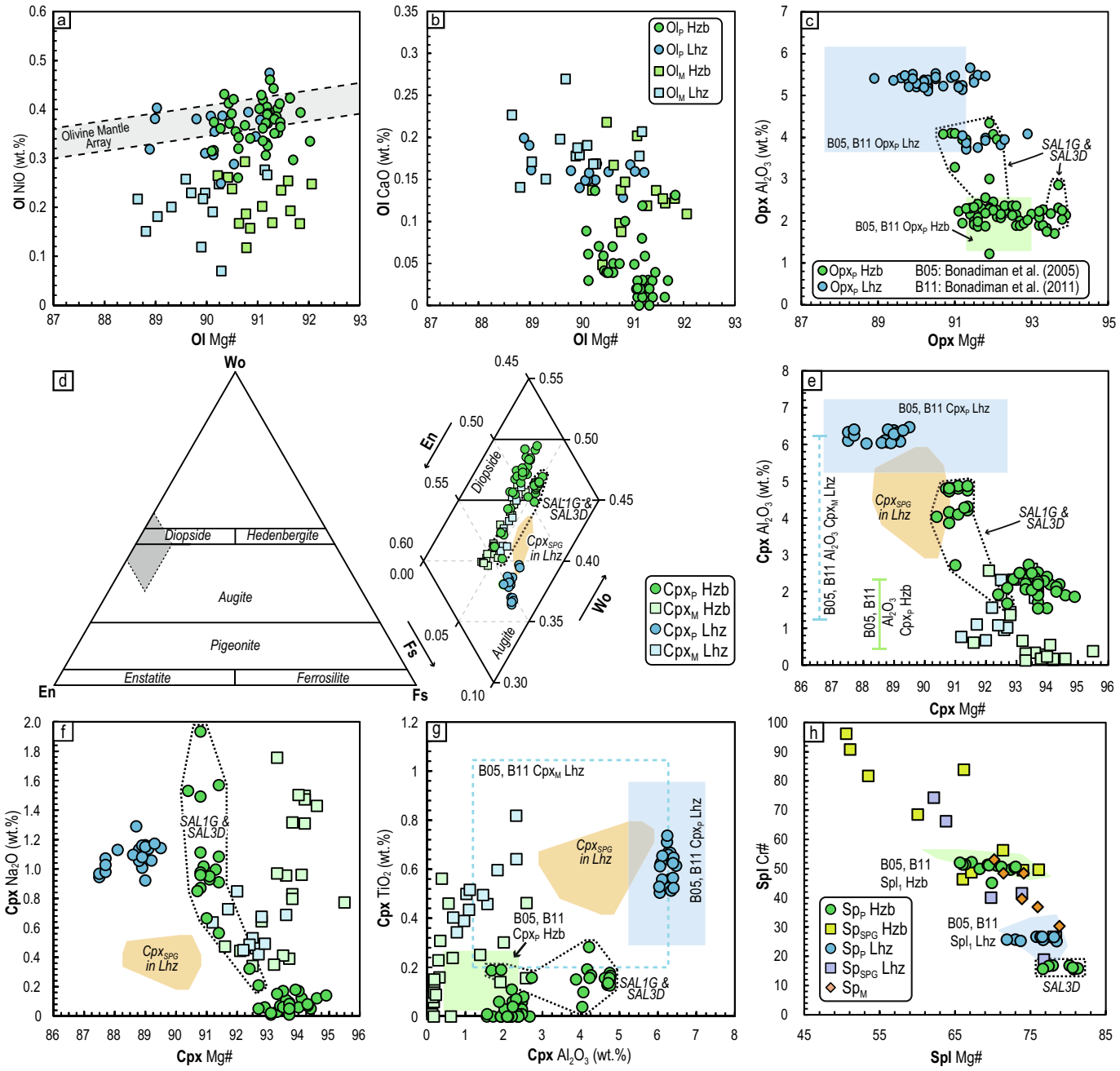

Fig. 7. Variation diagrams for olivine, orthopyroxene, clinopyroxene and spinel major elements composition. Light blue and green fields and dotted and continuous lines indicate the composition of clinopyroxenes, orthopyroxenes, and spinels from Bonadiman et al. (2005, 2011; B05: Bonadiman et al., 2005; B11: Bonadiman et al., 2011). The Olivine mantle array is from Takahashi (1986). Note how Cpx_{SPG} follows a different trend than that of Cpx_M. Hzb stands for harzburgite; Lhz stands for lherzolite.

Metasomatic reactions are particularly evident in harzburgites with low clinopyroxene content, where disequilibrium textures – such as tiny metasomatic olivine, clinopyroxene, spinel, and glass forming thick coronae around dissolving orthopyroxene porphyroclasts – are indicative of largely incomplete reactions between a metasomatic melt and orthopyroxene porphyroclasts (compare Figs. 2c and 3b, d). While the metasomatic phases exhibit the typical mineralogical trends associated with reactions involving Si-undersaturated melts, we do not observe enrichments in major and trace elements that would typically result from metasomatism by ultramafic silicate melts rich in alkalies. Instead, the major and trace element compositions of primary Mg-augite in harzburgites, metasomatic coronae, and microveins suggest that the metasomatism might have been influenced by carbonate-rich melts (Yaxley et al., 1991, 1998; Rudnick et al., 1993; Kogarko et al., 1995; Ionov et al., 1996). Mg-augite has low Ti and Al contents but high Mg#, Na and Cr contents. Moreover, the Cr# of Sp_M and Ca in Ol_M are high. The trace-element composition is characterised by enrichments in LILE, LREE, and Sr, and substantial depletion of HFSE. The Ti/Eu vs La_N/Yb_N ratios range approximately from 3000 to 4700 for Ti/Eu and from about 4.7 to 7.4 for La_N/Yb_N. Such intermediate Ti/Eu vs La_N/Yb_N ratios between carbonatitic and silicate melt metasomatic signatures indicate metasomatism by mixed silicate-carbonate melts (Fig. 11d; Green and Wallace, 1988; Rudnick et al., 1993; Yaxley et al., 1998; Coltorti et al., 1999; Hammouda and Laporte, 2000; Uenver-Thiele et al., 2017).

Direct evidence of the melts responsible for metasomatism is preserved in Type I and Type II inclusions and microveins. Type I

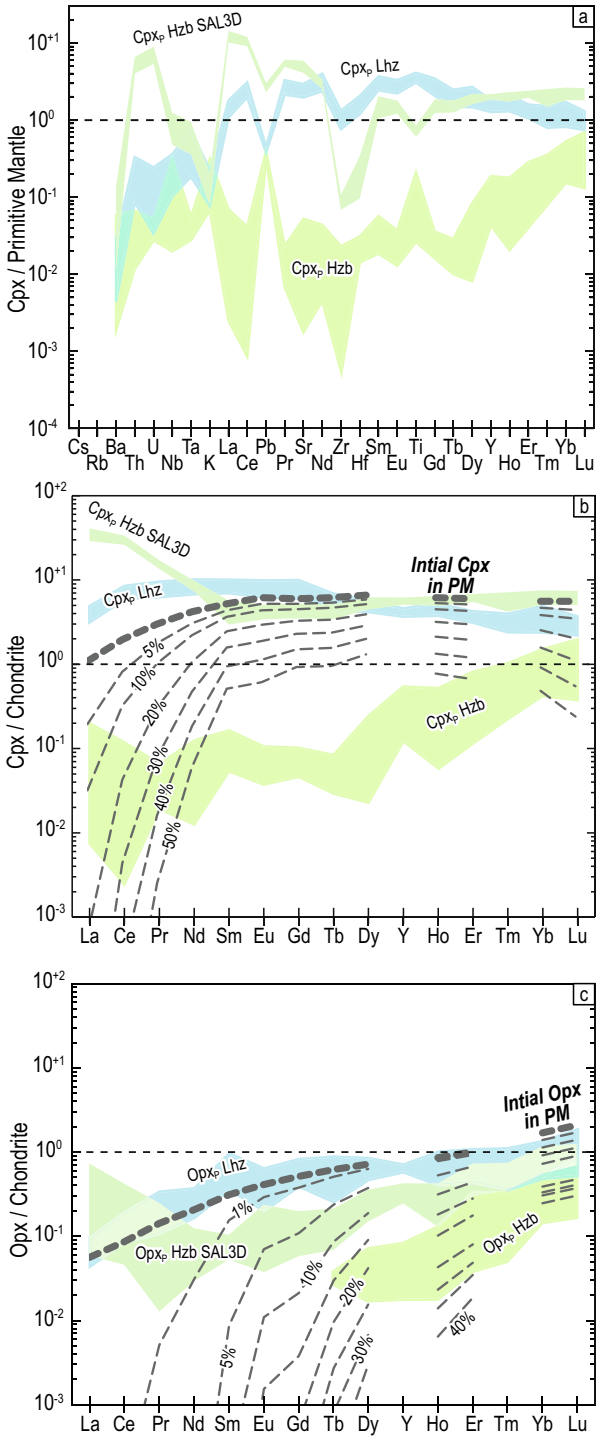

Fig. 8. Trace element spider diagrams of Cpx_P and Opx_P in harzburgites, including sample SAL3D, and lherzolites and normalised to the Primitive Mantle (Palme and O'Neill, 2014) and Chondrite (Palme and O'Neill, 2014). Mantle melting degrees are modelled as modal fractional melting (Shaw, 2006). The starting composition of fertile Cpx and Opx of the Primitive Mantle is computed from mass balance by using mineral-peridotite partition coefficients from McKenzie and O'nions (1991) and assuming a fertile spinel mantle derived from Palme and O'Neill (2014). The used mineral-melt partition coefficients for Cpx and Opx are from the compilation table 7 of Ionov et al. (2002). Mineral abbreviations as in Fig. 2. Hzb stands for harzburgite; Lhz stands for lherzolite.

inclusions record infiltration by a silicate-carbonate melt. These inclusions, hosted in olivine, consist of volatile-rich phonolitic to rhyolitic glass, carbonates, and a CO_2-(CO)-N_2 fluid phase. The silicate glass shows high concentrations of SiO_2 (57.5 – 69.6 wt.%), Al_2O_3 (14.9 – 21.0 wt.%), Na_2O (5.2 – 9.0 wt.%), K_2O (7.1 – 7.9 wt.%), and Cl (up to 4600 ppm). Associated carbonate phases include dolomite, Mg-calcite, calcite, and aragonite. Carbonates are also enriched in Cl (up to 2910 ppm), S (SO_3 up to 3740 ppm), and F (up to 2640 ppm), supporting their origin from an alkali-, volatile-, and carbonate-rich melt. Type I inclusions thus represent the earliest record of metasomatic agents in the deep lithosphere.

Type II inclusions, hosted in relic orthopyroxene near Cpx + Ol + Sp + Gl reaction coronas, indicate a more evolved stage of metasomatism, where carbonate–silicate melts react with orthopyroxene to form Cpx, Ol, Sp, and release CO_2, as shown by classical experimental (e.g., Green and Wallace, 1988; Yaxley et al., 1998) and natural (Rudnick et al., 1993) observations. These inclusions consist of silicate glass, CO_2-rich fluid, and daughter minerals (Cpx, Ol, apatite, whitlockite, brianite), but notably lack carbonates. At this stage, the silicate glass shows strong enrichment in K_2O (4.1 – 12.3 wt.%) and depletion in Na_2O and volatiles, while other major elements remain fairly constant. The reduction in volatile content and absence of carbonates reflect degassing during reaction with orthopyroxene, marking a more advanced stage of metasomatic evolution. The plot of silicate glass composition on an ASI vs AI diagram (Fig. 12c) reveals a linear trend among melt compositions of both Type I and II inclusions. This trend indicates evolution from moderately peralkaline phonolites and rhyolites to peraluminous trachytes. The primary driver of this trend is the decoupling of alkalies: K_2O increases sharply, while Na_2O decreases steadily, with Al_2O_3 remaining relatively constant. This pattern likely results from the crystallisation of metasomatic Mg-augite with the observed increase in aegirine component, characterised by high Na_2O and low Al_2O_3 content, in harzburgites.

In contrast, "primary" Mg-augite (7 – 13 vol.%) in lherzolites is rich in Al_2O_3 and TiO_2 and has low Mg#, in disequilibrium with the relatively high Mg# of Ol and Opx. Additionally, incompatible trace elements and REE abundances in lherzolite Mg-augite are comparable to, or even exceed, those in the clinopyroxene of a primordial mantle reservoir (Fig. 8). The Ti/Eu ratios are quite high, as are La_N/Yb_N ratios (Fig. 11d). These characteristics indicate that lherzolites mostly record metasomatic refertilisation by silica-undersaturated silicate melts. This silicate metasomatism essentially obliterated the chemical signature of carbonate–silicate metasomatism. Evidence for carbonate–silicate metasomatism in lherzolites is locally preserved only in Cpx_M, Ol_M and Sp_M in intergranular microveins and in both Type I and II inclusions.

Therefore, Sal Island peridotites record a multi-stage metasomatic evolution. Silicate melts rich in carbonate, volatiles, and incompatible elements – i.e., proximal to carbonatitic composition – have percolated into the lithospheric mantle from depths greater than 106 km.

Metasomatism at this stage does not significantly modify the paragenesis (Opx ≫ Cpx) or the major-element chemistry of rocks, but considerably enriches and fractionates the incompatible elements' budget. This is evident in the nearly fourfold increase in the La_N/Yb_N ratio in metasomatised harzburgites (compare primary diopsides with Mg-augites in harzburgites in Fig. 11d).

Although the infiltration of carbonate-rich silicate melts in the lithosphere could ultimately lead to the conversion of harzburgites and lherzolites into orthopyroxene-free wehrlite (Yaxley et al., 1991; Dautria et al., 1992), wehrlites have not been observed among the studied peridotites; in harzburgites, metasomatic reactions appear to be frozen, and CO_2-rich fluids are exsolved. As previously discussed, wehrlitisation is irrelevant in the deep lithosphere, where extensive CO_2 degassing by orthopyroxene consumption and clinopyroxene production is considerably hindered (e.g., Kamenetsky and Yaxley, 2015; Stone and Luth, 2016; Sharygin et al., 2017; Aulbach et al., 2020; Yaxley et al., 2022).

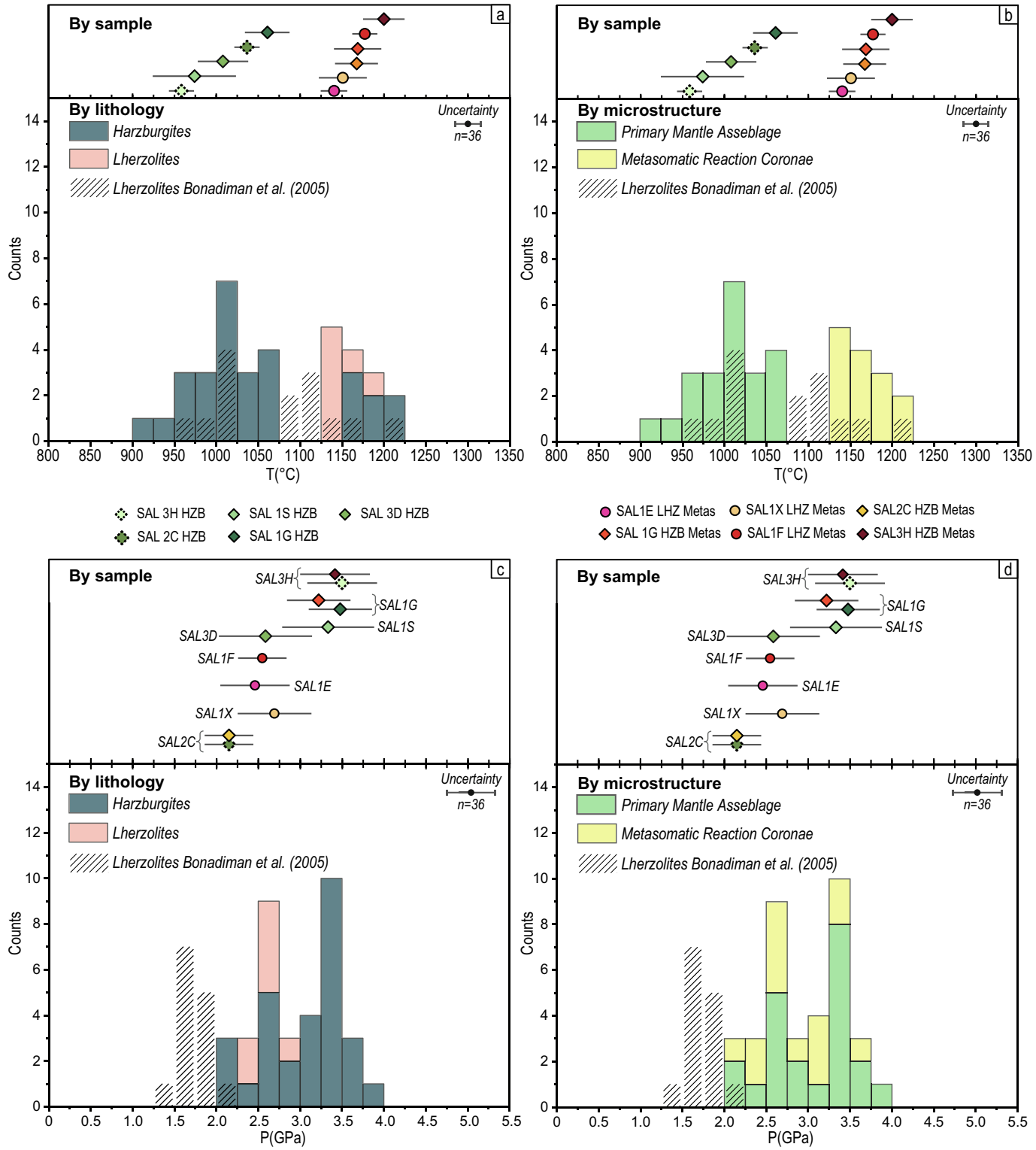

Fig. 9. Histograms reporting estimated temperatures and pressure distribution for analysed mantle xenoliths, with data based on sample, lithology and microstructures. In the upper plots of c and d, the pressure estimates of primary and metasomatic mineral assemblages are directly compared for each sample, showing the isobaric equilibration of metasomatic mineral assemblages relative to the primary one. The dashed areas represent literature data from the same locality from Bonadiman et al. (2005). The uncertainties reported for each calculation correspond to those reported in the literature.

At shallower depths, from approximately 70 – 80 km onward, that is above the carbonate ledge (e.g., Eggler, 1978a, 1978b; Dalton and Presnall, 1998), alkali- and aluminium-rich silicate melts, along with CO_2, enrich the rock chemistry and mineralogy in the Cape Verde mantle (e.g., Barker et al., 2023). As a result, the clinopyroxene content in most peridotites sampled at these depths increases, and peridotite chemistry approaches a primitive mantle composition. Although not conclusive, this evolution suggests that a single alkali-rich silicate-carbonate parent metasomatic melt evolved into alkali-rich silicate melt and CO_2 fluid on

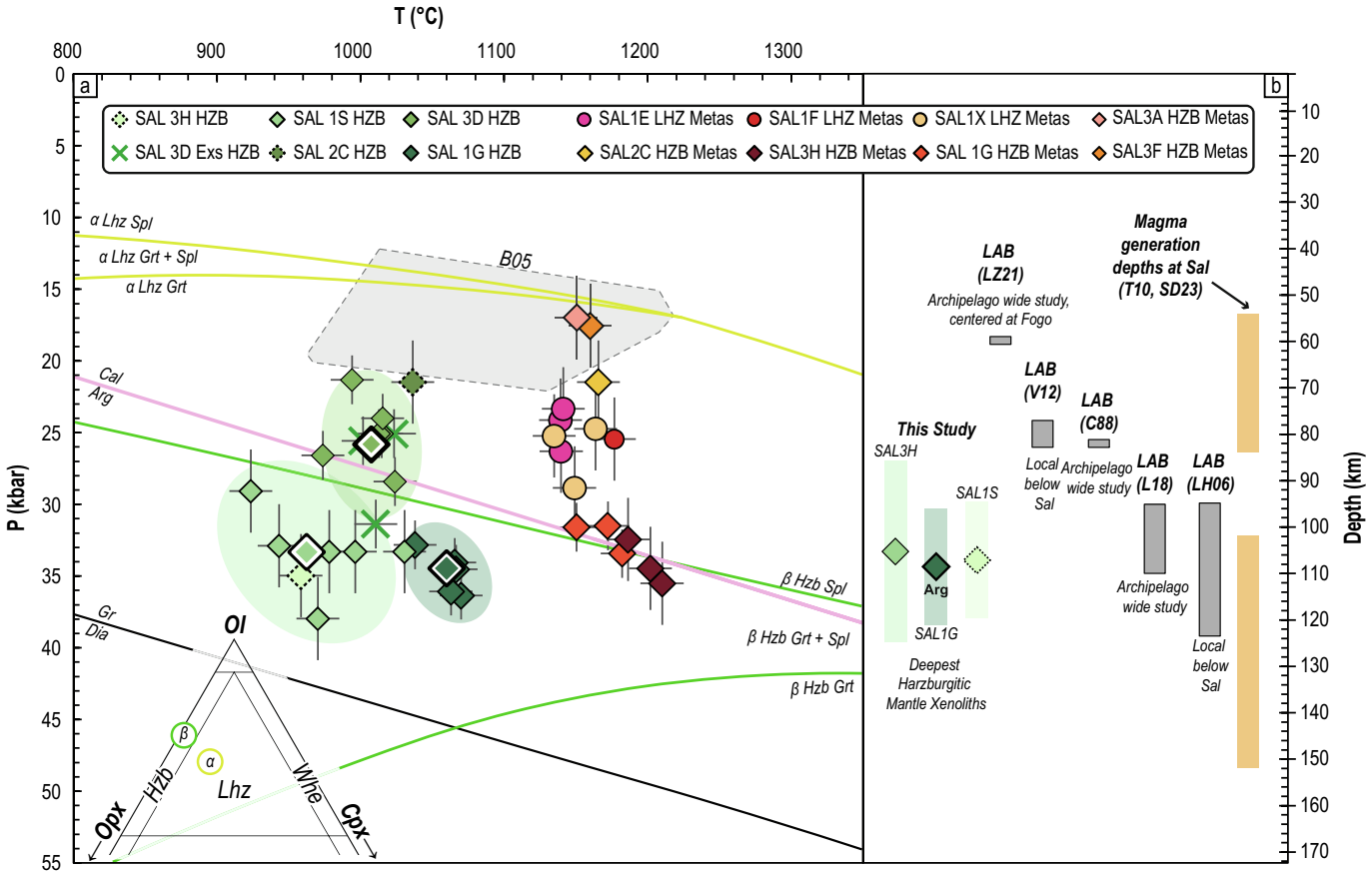

Fig. 10. (a) Estimated pressure and temperature conditions of equilibration of studied xenoliths. The aragonite-calcite transition is the experimentally calibrated curve of Zhao et al. (2019). The green curves represent the spinel/spinel-garnet/garnet facies pressure–temperature conditions calculated for two different mantle compositions representative of a fertile lherzolite (composition α) and a harzburgite (composition β). As a reference, the modal classification of the used peridotitic bulk composition is displayed in the inset on the left. The peridotitic bulk compositions from two selected mantle xenoliths are from Bonadiman et al. (2005) and are reported in Supplementary Data Table S3. A confidence ellipse with the average P-T estimate for each sample has been calculated for the primary mantle assemblage in harzburgites, the internal white border denotes the average of the sample estimates. The grey field represents the P-T condition of the xenoliths from Bonadiman et al. (2005), identified with B05. Peridotite spinel, spinel-garnet and garnet facies pressure–temperature boundaries were computed through free energy minimisation using Perple_X (version 7.1.6; Connolly, 2009) with condensed phase data (DS6.3.4) and solution models from Tomlinson and Holland (2021). (b) Comparison among the depth range constrained by the deepest harzburgitic xenoliths, indicating the minimum depth to which a depleted lithosphere is present, the lithosphere-asthenosphere boundary (LAB) position from various geophysical studies, and the primary magmas generation depths beneath Sal. C88: Cazenave et al. (1988); LH06: Lodge and Helffrich (2006); T10: Torres et al. (2010); V12: Vinnik et al. (2012); L18: Lodhia et al. (2018); LZ21: Liu and Zhao (2021); SD23: Sun and Dasgupta (2023). Sp stands for spinel; Grt stands for garnet; Cal stands for calcite; Arg stands for aragonite; Dia stands for diamond; Gr stands for graphite. Hzb stands for harzburgite; Lhz stands for lherzolite; Whe stands for wherlite. Exs stand for exsolution, and Metas stand for metasomatic.

ascent by progressive silica enrichment as a result of reaction with the deeper portion of the lithospheric mantle beneath Sal, differentiation processes, such as carbonate and phosphate crystallisation, and, eventually, extensive carbonate degassing above the carbonate ledge (~2.2 – 2.6 GPa, equivalent to ~ 70 – 80 km; Eggler, 1978a, 1978b; Dalton and Presnall, 1998), Alternatively, it may have occurred by carbonate–silicate immiscibility processes (e.g., Frezzotti et al., 2002a, 2002b; Berkesi et al., 2023), or by dilution with additional silicate components increasing melt volume.

8.3. On the nature of carbon-rich metasomatic agents

In the lithosphere and the underlying asthenosphere, silicate-carbonate melts can be generated by the melting of carbonated peridotites, carbonated eclogite, and carbonated metasediments (e.g., Dasgupta et al., 2006; Dasgupta et al., 2007; Thomsen and Schmidt, 2008; Gerbode and Dasgupta, 2010; Grassi and Schmidt, 2011; Tsuno and Dasgupta, 2011; Kiseeva et al., 2012). The composition of silicate glass in Type I and II inclusions differs from that of melts produced by carbonated peridotite melting (Fig. 12a, b). Experimental melts from carbonated peridotites typically show higher Mg and Ca contents in the silicate component, along with significantly lower alkalies – in particular K – and Ti concentrations (Dasgupta et al., 2007; Fig. 12a and b). Also, carbonates in type I inclusions and microveins are less Mg-rich (on average MgO = 3.7 wt.%) than carbonates in peridotite melting experiments (i.e., ~13 – 14 wt.%; Dasgupta et al., 2007). While these characteristics do not rule out an origin from low degrees of melting of a carbonated peridotite, the high K_2O/TiO_2 ratios in the silicate glass suggest the involvement of a melt component derived from recycled carbonated lithologies, such as metasediments and/or eclogites. At Sal Islands, metasomatic silicate-carbonate melts show a major element composition indicative of a significant contribution from recycled carbonated sediments (GL_{INC}; compare carbonated sediment melts and carbonated eclogite and carbonated peridotite melts in Fig. 12a, b). Silicate-carbonate melts from sediments at P of 3.0 – 5.0 GPa and T of 1150 – 1350 °C are Ca-, Na-, and K-rich and contain 7.2 wt.% to 9.2 wt.% CO_2 as carbonate (Thomsen and Schmidt, 2008; Grassi and Schmidt, 2011; Tsuno and Dasgupta, 2011). A further contribution from carbonated eclogite melts could explain the high Ti content in some glass compositions (Gerbode and Dasgupta, 2010; Kiseeva et al., 2012). Additionally, silicate

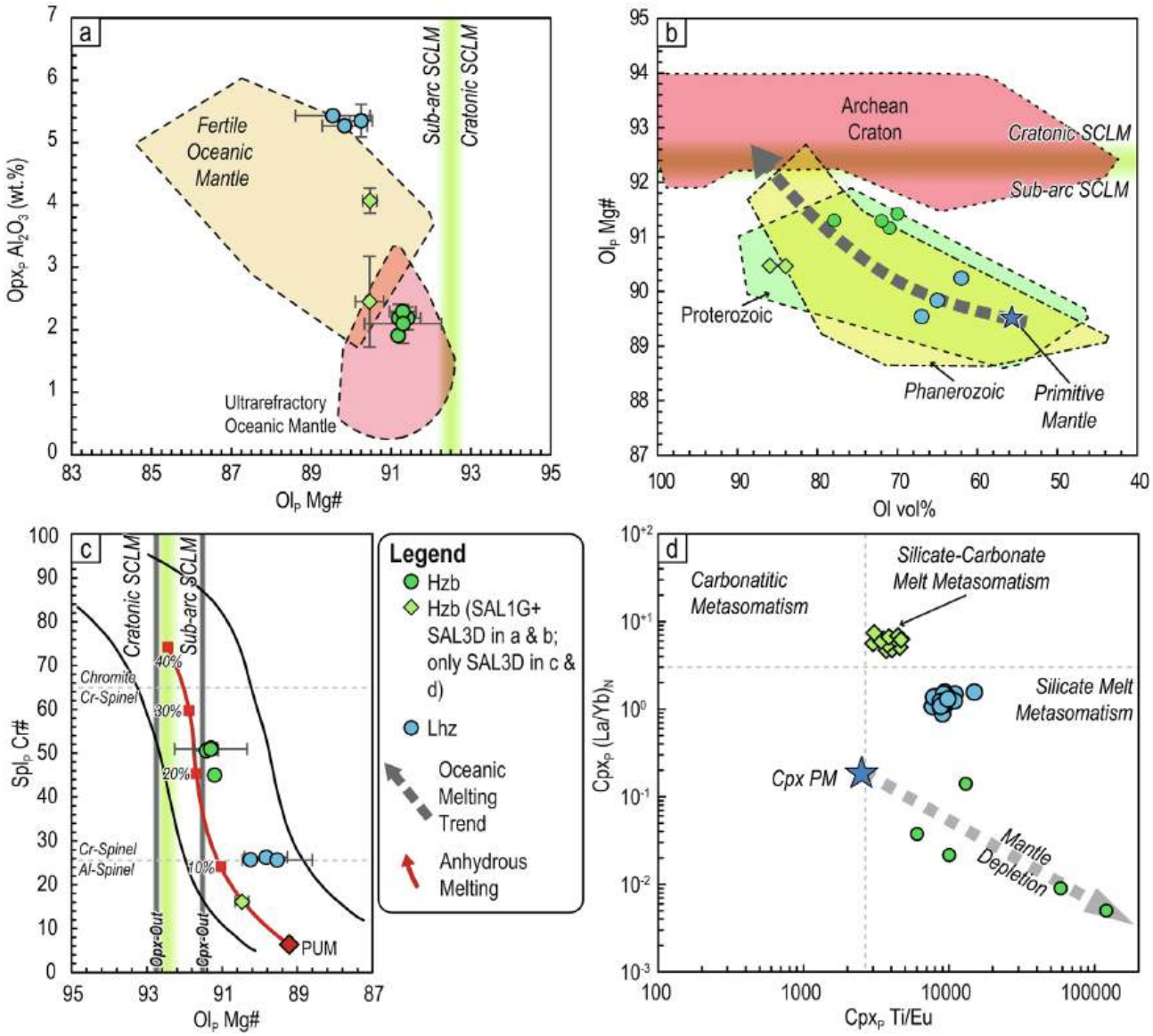

Fig. 11. (a) Al_2O_3 in Opx vs Mg# in Ol discriminating between Ferile and Ultradepleted Oceanic Mantle (Simon et al., 2008). (b) Boyd Plot (Boyd, 1989) of olivine vol.% and average olivine Mg#. Fields modified following Bernstein et al. (2006). In (a, b and c), the wide boundary between Cratonic and Sub-arc SCLM Mg# composition of olivine has been derived from data reported in Boyd (1989), Pearson et al. (2003), Bernstein et al. (2006) and Neumann and Simon (2009). (c) Olivine-Spinel Mantle Array (OSMA; Arai, 1994) plot. The orthopyroxene-out and clinopyroxene-out for melting and boundaries for the spinel composition and the spinel composition divides are from Scott et al. (2019) and references therein. (d) Plot of Ti/Eu vs chondrite-normalised La/Yb in clinopyroxene (Coltorti et al., 1999). The rough location of silicate-carbonate melt metasomatism is from Uenver-Thiele et al. (2017). The Primitive Mantle (PM) Cpx composition was obtained following the same procedure as in Fig. 8b. Hzb stands for harzburgite; Lhz stands for lherzolite. SCLM stands for Subcontinental Lithospheric Mantle. Mineral abbreviations as in Fig. 2.

glass and carbonates are enriched in Cl, N, S, and P, which are abundant in deep metasediments (Barnes et al., 2018; Frezzotti and Ferrando, 2018; Scambelluri et al., 2019; Li et al., 2020; Harris et al., 2022).

This finding agrees with the isotope geochemistry data from magmas. At Cape Verde, several authors have suggested that the isotopic signature of magmas reflects a hybrid mantle reservoir containing both primordial and recycled components, such as subducted carbonate-rich crustal lithologies (Gerlach et al., 1988; Hoernle et al., 2002; Doucelance et al., 2003, 2010; Holm et al., 2006; Barker et al., 2010, 2014; Martins et al., 2010; Villaseca et al., 2025). In particular, the HIMU isotopic signature is mainly attributed to the recycling and ageing of altered oceanic crust. Additionally, the EM1 isotopic signature of southern and eastern archipelago magmas is considered to involve contributions from recycled sediments, although it may also indicate interaction with subcontinental lithospheric mantle. The heavy $\delta^{13}C$ (–0.4‰) for CO_2 from undegassed magmas from Fogo and the Ca light marine carbonate-like isotope signature in carbonatites from Brava islands further support the involvement of sedimentary carbon (Amsellem et al., 2020; Lo Forte et al., 2024b).

8.4. Geodynamic carbon enrichment of the lithosphere beneath Cape Verde

A significant question is how the carbon-rich crustal components might have been preserved at sub-lithospheric depths. The geographical location of the Cape Verde archipelago (Fig. 1a) may help explain the continental off-craton nature of the lithospheric roots beneath Sal and the deep carbon enrichment processes

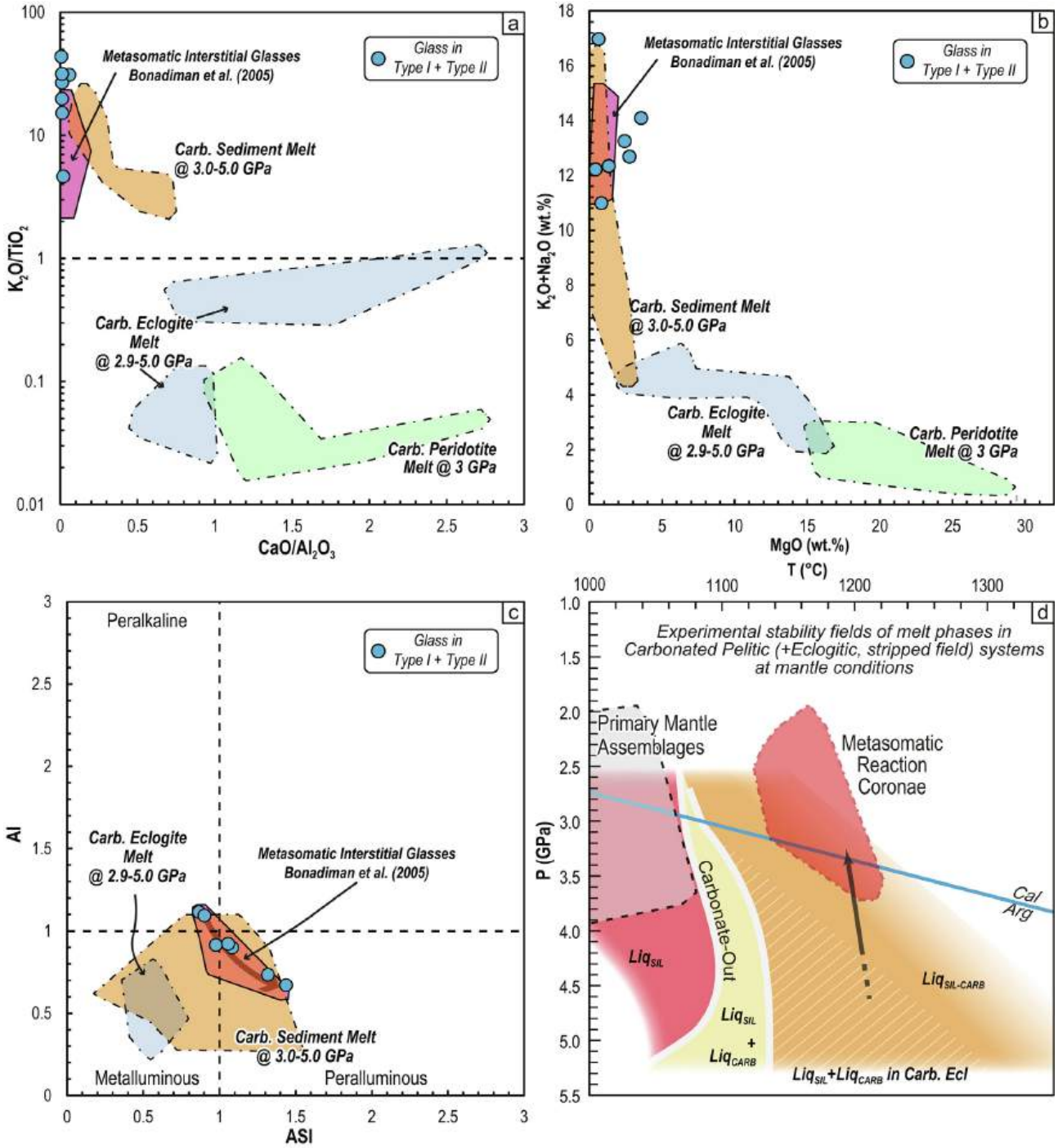

Fig. 12. (a, b, c) Variation diagrams comparing GL_{INC} (i.e., glass in Type I and II inclusions) and data from Bonadiman et al. (2005) with experimental melts from: Thomsen and Schmidt (2008), Tsuno and Dasgupta (2011), Grassi and Schmidt (2011) for carbonated pelites and calcareous pelites, from Dasgupta et al. (2006), Gerbode and Dasgupta (2010) for carbonated eclogites and from Dasgupta et al. (2007) and Kiseeva et al. (2012) for carbonated peridotites. (d) Experimentally determined stability fields of silicate, immiscible silicate, and carbonatitic melts and miscible chiefly for silicate-carbonate melt for carbonated sedimentary and eclogitic systems from Thomsen and Schmidt (2008) and Kiseeva et al. (2012). ASI stands for Allumina Saturation Index; AI stands for Alkalinity Index.

revealed by the present study. Since the Neoproterozoic, this margin of the West African Craton has witnessed multiple subduction and collision events during both the Neoproterozoic to Cambrian Pan-African orogenic cycles and the closure and subduction of the Rheic Ocean in Devonian to Permian times (370 – 280 Ma), on the assembly of Pangea (e.g., Villeneuve and Marcaillou, 2013; Villeneuve et al., 2024, and references therein). Recycled components could have been introduced and stored in the mantle during one or more subduction events that have taken place west of the West African Craton. Such a rough age for the formation of such a reservoir would align with the modelled age (400 Ma) of the recycled sedimentary component in OIB magmas (Doucelance et al., 2010).

These processes suggest carbon storage occurs over time below the lithosphere-asthenosphere boundary (LAB) at depths shallower than roughly 180 km, where conditions are sufficiently oxidised to

enable carbonate stability, above the EMOD/G oxygen buffer (Enstatite-Magnesite-Olivine-Diamond/Graphite; Stagno and Frost, 2010; Stagno et al., 2013; Luth and Stachel, 2014). Notably, our data emphasise the involvement of carbonate-rich metasediments, which are known to form diapirs that tend to reach the base of the lithosphere (Ducea et al., 2022). This enriched carbon reservoir in the shallow mantle beneath the archipelago, which formed sometime between the Neoproterozoic Pan African Orogeny and the Permian closure of the Rheic Ocean, has been primed for reactivation at any time by geodynamic events (e.g., Malusà et al., 2018; Tamburello et al., 2018), whether related to tectonics or a rising plume (Courtillot et al., 2003; Anderson, 2005; Fig. 13).

Undegassed magmas from Cape Verde contain high levels of CO_2, ranging from 2.0 wt.% to 2.7 wt.% at ~ 0.8 – 1.0 GPa (DeVitre et al., 2023; Lo Forte et al., 2024a). According to the modelling by Sun and Dasgupta (2023), Cape Verde primitive magmas at the source are predicted to be among the richest in CO_2 within the OIB magmas, with an average CO_2 content of 9.12 ± 1.78 wt. % at 3.9 4.3 GPa. Following their modelling approach (see Supplementary Data), it is estimated that approximately 2788 ± 544 ppm of CO_2 should be present in the Cape Verde mantle source. Notably, the estimated average CO_2 content of the OIB mantle plume is considerably lower, ranging from about 1240 to 1467 ppm of CO_2 (Sun and Dasgupta, 2023; Dasgupta and Aubaud, 2025) to around ~ 1550 – 1750 ppm of CO_2 at roughly 100 – 120 km of depth (Aiuppa et al., 2021). This discrepancy supports the possibility of an additional carbon reservoir in the upper mantle beneath Cape Verde.

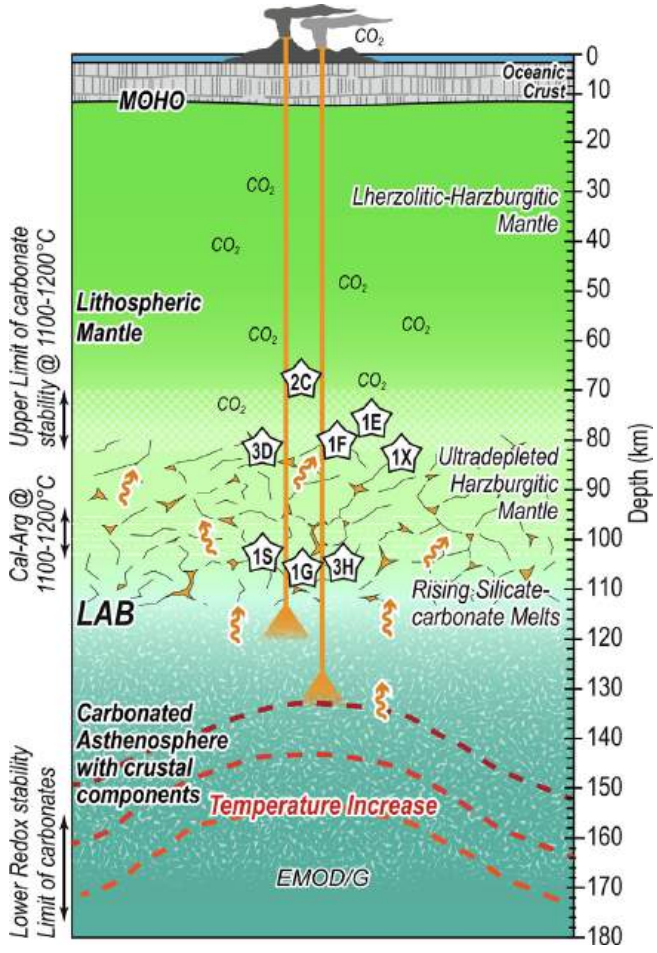

Fig. 13. Sketch depicting the inferred upper mantle structure, the locus of the relevant metasomatic processes due to rising silicate-carbonate melt from the carbonated and crustal component-bearing asthenosphere beneath Sal island around the time of mantle xenoliths entrainment in erupting lavas (i.e., ~11 Ma). The depth of the carbonate "ledge", where CO_2 instead of carbonate becomes stable, and the aragonite-calcite transition at temperatures likely present during metasomatism, are also reported for reference. The extent of the carbonated and crustal component-bearing asthenosphere is loosely drawn from experiments (e.g., Stagno and Frost, 2010; Stagno et al., 2013; Luth and Stachel, 2014). White stars indicate the sampling depths of the studied xenoliths. EMOD/G stands fro Enstatite-Magnesite-Olivine-Diamond/Graphite.

Hoernle et al. (2002) and Doucelance et al. (2010) proposed that the isotopic characteristics of Cape Verde magmas could be explained by the addition of 3 wt.% of old (1.6 Gyr to 0.4 Gyr) metasedimentary and eclogitic components to the Cape Verde mantle source (Fig. 13). By mass-balancing the addition of 3 wt.% of a recycled metasomatic silicate-carbonate component, containing from 7.2 wt.% to 9.2 wt.% of CO_2 (averaging around 7.8 wt.%; Thomsen and Schmidt, 2008; Grassi and Schmidt, 2011; Tsuno and Dasgupta, 2011), it is observed that metasomatic melts could contribute up to $5.0^{+0.6}_{-0.5}$ kg of CO_2 per m^3 of peridotite. This contribution would further increase the carbon budget of the Cape Verde asthenospheric mantle by 1930^{+243}_{-102} ppm, effectively doubling the CO_2 budget of the average OIB mantle source proposed by Sun and Dasgupta (2023).

The melting of carbonate peridotite begins when the mantle temperature exceeds the carbonated mantle solidus, resulting in a melt fraction that depends on the amount of CO_2 present in the mantle (Dasgupta et al, 2013). At the CO_2 concentrations proposed for the OIB mantle, it could generate sufficient carbonate–silicate melt to form an interconnected network of melts in the asthenosphere, constrained at its base only by redox freezing (Stagno et al., 2013). Once generated, carbonate melt components are highly mobile and can infiltrate the lithosphere, migrating along grain boundaries and inducing metasomatic reactions, primarily through the dissolution of orthopyroxene, thereby gradually enriching the lithosphere in CO_2 (e.g., Kamenetsky and Yaxley, 2015; Stone and Luth, 2016; Sharygin et al., 2017). CO_2 fluids, in contrast, have significantly lower mobility and tend to remain in rocks (Frezzotti and Touret, 2014) along grain boundaries, which can be tapped by rising magmas.

9. Conclusions

This study investigates the processes of carbon enrichment in the chemically heterogeneous lithospheric mantle beneath Sal Island, Cape Verde, which consists of ultradepleted spinel harzburgites and spinel lherzolites. The harzburgites are characterised by high degrees of partial melting (20% – 40%), as indicated by high modal olivine content, elevated Mg#, very low clinopyroxene abundance, and depleted signatures of incompatible elements. The primary mantle mineral assemblages have equilibrated at temperatures ranging from approximately 950 to 1060 °C at 66 to 106 km depth. Metasomatic processes occurred at higher temperatures, between 1140 and 1200 °C. Evidence of metasomatism is observed in reaction coronae, which consist of tiny grains of olivine, clinopyroxene, spinel, and interstitial glass, surrounding dissolving orthopyroxene as a result of interaction with an infiltrating melt. Enrichments in major and trace elements in clinopyroxene in harzburgites and lherzolites suggest at least two significant metasomatic events involving alkali-rich silicate-carbonate melts and CO_2– and alkali-rich silicate melts. These metasomatic carbonate-rich melts contain recycled subducted components, specifically carbonated sediments and eclogites. Clear evidence of carbonate–silicate melt infiltrating the deep lithosphere is observed in the melt and fluid within inclusions and microveins.

Our findings evidence the major control of regional geodynamics in carbon enrichment processes beneath the Cape Verde archi-

pelago, governing carbon transport to the asthenosphere through the multiple subduction and collision events that affected this western margin of the West African Craton and creating carbonate-enriched domains over millions to billions of years. Reactivation by upwelling of the carbonated asthenosphere produced carbonate-rich silicate melts that migrated upward and metasomatised the overlying thick lithospheric mantle. A significant outcome of metasomatism is deep lithospheric CO_2 degassing. These processes significantly contribute to the carbon budget of the upper mantle beneath the Cape Verde Islands, which is the source of OIB magmas.

CRediT authorship contribution statement

Andrea Maffeis: Writing – review & editing, Writing – original draft, Visualization, Methodology, Investigation, Formal analysis, Data curation. **Maria Luce Frezzotti:** Writing – review & editing, Writing – original draft, Supervision, Resources, Project administration, Methodology, Funding acquisition, Conceptualization. **Rosario Esposito:** Writing – review & editing, Methodology, Investigation. **Marco G. Malusà:** Writing – review & editing, Validation. **Alessandro Aiuppa:** Writing – review & editing, Resources. **Andrea Luca Rizzo:** Writing – review & editing, Resources. **Simona Ferrando:** Writing – review & editing, Validation, Supervision, Investigation.

Declaration of competing interest

The authors declare that they have no known competing financial interests or personal relationships that could have appeared to influence the work reported in this paper.

Acknowledgements

We thank Andrea Risplendente and Gianluca Sessa for their support during EPMA and LA-ICP-MS analyses. This work was supported by the Italian Ministry of University and Research (PRIN 2022, project no. 2022HA8XCS) to M.L.F.. Abigail Barker and Joao Mata are kindly thanked for their insightful comments that helped improve the manuscript, as well as the editorial handling of Associate Editor Kristoffer Szilas.

Appendix A. Supplementary data

Supplementary data to this article can be found online at https://doi.org/10.1016/j.gsf.2025.102179.

References

Aiuppa, A., Casetta, F., Coltorti, M., Stagno, V., Tamburello, G., 2021. Carbon concentration increases with depth of melting in Earth's upper mantle. Nat. Geosci. 14 (9), 697–703.

Amsellem, E., Moynier, F., Bertrand, H., Bouyon, A., Mata, J., Tappe, S., Day, J.M., 2020. Calcium isotopic evidence for the mantle sources of carbonatites. Sci. Adv. 6 (23), eaba3269.

Anderson, D. L., 2005. Scoring hotspots: The Plume and Plate Paradigms. In: Foulger, G. R., Natland J. H., Presnall D. C., D. L. Anderson (Eds.), Plates, Plumes, and Paradigms. Geological Society of America 388, pp. 31–54.

Arai, S., 1994. Characterization of spinel peridotites by olivine-spinel compositional relationships: review and interpretation. Chem. Geol. 113 (3–4), 191–204.

Aulbach, S., Lin, A.B., Weiss, Y., Yaxley, G.M., 2020. Wehrlites from continental mantle monitor the passage and degassing of carbonated melts. Geochem. Perspect. Lett. 15, 30–34.

Barker, A.K., Holm, P.M., Peate, D.W., Baker, J.A., 2010. A 5 million year record of compositional variations in mantle sources to magmatism on Santiago, southern Cape Verde archipelago. Contrib. Mineral. Petrol. 160, 133–154.

Barker, A.K., Holm, P.M., Troll, V.R., 2014. The role of eclogite in the mantle heterogeneity at Cape Verde. Contribut. Mineral. Petrol. 168, 1–15.

Barker, A.K., Rydeblad, E.M., Silva, S.M., 2021. Magma storage at ocean islands: Insights from Cape Verde. In: Masotta, M., Beier, C., Mollo, S. (Eds.), Crustal Magmatic System Evolution: Anatomy, Architecture, and Physico-Chemical Processes. American Geophysical Union, pp. 45–78.

Barker, A.K., Magnusson, E., Troll, V.R., Harris, C., Mattsson, H.B., Holm, P.M., Perez-Torrado, F.J., Carracedo, J.C., Deegan, F.M., 2023. Disequilibrium in historic volcanic rocks from Fogo, Cape Verde traces carbonatite metasomatism of recycled ocean crust. Lithos 456, 107328.

Barnes, J.D., Manning, C.E., Scambelluri, M., Selverstone, J., 2018. The Behavior of Halogens During Subduction-Zone Processes. In: Harlov, D., Aranovich, L. (Eds.), The Role of Halogens in Terrestrial and Extraterrestrial Geochemical Processes. Springer Geochemistry, Springer, Cham, pp. 545–590.

Begg, G.C., Griffin, W.L., Natapov, L.M., O'Reilly, S.Y., Grand, S.P., O'Neill, C.J., Hronsky, J.M.A., Poudjom Djomani, Y., Swain, C.J., Deen, T., Bowden, P., 2009. The lithospheric architecture of Africa: Seismic tomography, mantle petrology, and tectonic evolution. Geosphere 5 (1), 23–50.

Berkesi, M., Myovela, J.L., Yaxley, G.M., Guzmics, T., 2023. Carbonatite formation in continental settings via high pressure–high temperature liquid immiscibility. Geochim. Cosmochim. Acta 349, 41–54.

Bernstein, S., Hanghøj, K., Kelemen, P.B., Brooks, C.K., 2006. Ultra-depleted, shallow cratonic mantle beneath West Greenland: dunitic xenoliths from Ubekendt Ejland. Contribut. Mineral. Petrol. 152, 335–347.

Boyet, M., Doucelance, R., Israel, C., Bonnand, P., Auclair, D., Suchorski, K., Bosq, C., 2019. New constraints on the origin of the EM-1 component revealed by the measurement of the La-Ce isotope systematics in Gough Island lavas. Geochem. Geophys. Geosyst. 20, 2484–2498.

Bonadiman, C., Beccaluva, L., Coltorti, M., Siena, F., 2005. Kimberlite-like metasomatism and "garnet signature" in spinel-peridotite xenoliths from Sal, Cape Verde Archipelago: relics of a subcontinental mantle domain within the Atlantic oceanic lithosphere? J. Petrol. 46 (12), 2465–2493.

Bonadiman, C., Coltorti, M., Beccaluva, L., Griffin, W.L., O'Reilly, S.Y., Siena, F., 2011Lithosphere, 2011. Metasomatism versus host magma infiltration: A case study of Sal mantle xenoliths, Cape Verde Archipelago. In: Beccaluva, L., Bianchini, G., Wilson, M. (Eds.). Geol. Soc. Am. 478, 283–305.

Boyd, F.R., 1989. Compositional distinction between oceanic and cratonic lithosphere. Earth Planet. Sci. Lett. 96 (1–2), 15–26.

Brey, G.P., Köhler, T., 1990. Geothermobarometry in four-phase lherzolites II. New thermobarometers, and practical assessment of existing thermobarometers. J. Petrol. 31 (6), 1353–1378.

Carvalho, J., Bonadio, R., Silveira, G., Lebedev, S., Mata, J., Arroucau, P., Meier, T., Celli, N.L., 2019. Evidence for high temperature in the upper mantle beneath Cape Verde archipelago from Rayleigh-wave phase-velocity measurements. Tectonophysics 770, 228225.

Carvalho, J., Silveira, G., Kiselev, S., Custódio, S., Ramalho, R.S., Stutzmann, E., Schimmel, M., 2022. Crustal and uppermost mantle structure of Cape Verde from ambient noise tomography. Geophys. J. Int. 231 (2), 1421–1433.

Castillo, P.R., 2015. The recycling of marine carbonates and sources of HIMU and FOZO ocean island basalts. Lithos 216, 254–263.

Cazenave, A., Souriau, A., Dominh, K., 1988. Global coupling of Earth surface topography with hotspots, geoid and mantle heterogeneities. Nature 340 (6228), 54–57.

Chauvel, C., Hofmann, A.W., Vidal, P., 1992. HIMU-EM: the French Polynesian connection. Earth Planet. Sci. Lett. 110 (1–4), 99–119.

Coltorti, M., Bonadiman, C., Hinton, R.W., Siena, F., Upton, B.G.J., 1999. Carbonatite metasomatism of the oceanic upper mantle: evidence from clinopyroxenes and glasses in ultramafic xenoliths of Grande Comore, Indian Ocean. J. Petrol. 40 (1), 133–165.

Coltorti, M., Bonadiman, C., O'Reilly, S.Y., Griffin, W.L., Pearson, N.J., 2010. Buoyant ancient continental mantle embedded in oceanic lithosphere (Sal Island, Cape Verde Archipelago). Lithos 120 (1–2), 223–233.

Connolly, J.A.D., 2009. The geodynamic equation of state: what and how. Geochem. Geophys. Geosyst. 10 (10), Q10014.

Courtillot, V., Davaille, A., Besse, J., Stock, J., 2003. Three distinct types of hotspots in the Earth's mantle. Earth Planet. Sci. Lett. 205 (3–4), 295–308.

Dalton, J.A., Presnall, D.C., 1998. Carbonatitic melts along the solidus of model lherzolite in the system CaO-MgO-Al_2O_3-SiO_2-CO_2 from 3 to 7 GPa. Contribut. Mineral. Petrol. 131, 123–135.

Dasgupta, R., Hirschmann, M.M., 2010. The deep carbon cycle and melting in Earth's interior. Earth Planet. Sci. Lett. 298 (1–2), 1–13.

Dasgupta, R., Aubaud, C., 2025. Major volatiles in the Earth's mantle beneath mid-ocean ridges and intraplate ocean islands. In: Anbar, A., Weis, D. (Eds.), Treatise on Geochemistry (3rd Edition). Elsevier, pp. 381–423.

Dasgupta, R., Hirschmann, M.M., Stalker, K., 2006. Immiscible transition from carbonate-rich to silicate-rich melts in the 3 GPa melting interval of eclogite +CO_2 and genesis of silica-undersaturated ocean island lavas. J. Petrol. 47 (4), 647–671.

Dasgupta, R., Hirschmann, M.M., Smith, N.D., 2007. Partial melting experiments of peridotite+CO_2 at 3 GPa and genesis of alkalic ocean island basalts. J. Petrol. 48 (11), 2093–2124.

Dasgupta, R., Mallik, A., Tsuno, K., Withers, A.C., Hirth, G., Hirschmann, M.M., 2013. Carbon-dioxide-rich silicate melt in the Earth's upper mantle. Nature 493 (7431), 211–215.

Dautria, J.M., Dupuy, C., Takherist, D., Dostal, J., 1992. Carbonate metasomatism in the lithospheric mantle: peridotitic xenoliths from a melilititic district of the Sahara basin. Contribut. Mineral. Petrol. 111, 37–52.

de Ignacio, C., Muñoz, M., Sagredo, J., 2012. Carbonatites and associated nephelinites from São Vicente, Cape Verde Islands. Mineral. Magaz. 76 (2), 311–355.
DeVitre, C.L., Gazel, E., Ramalho, R.S., Venugopal, S., Steele-MacInnis, M., Hua, J., Allison, C.M., Moore, L.R., Carracedo, J.C., Monteleone, B., 2023. Oceanic intraplate explosive eruptions fed directly from the mantle. Proc. Nat. Acad. Sci. 120 (33), e2302093120.
Doucelance, R., Escrig, S., Moreira, M., Gariépy, C., Kurz, M.D., 2003. Pb-Sr-He isotope and trace element geochemistry of the Cape Verde Archipelago. Geochim. Cosmochim. Acta 67 (19), 3717–3733.
Doucelance, R., Hammouda, T., Moreira, M., Martins, J.C., 2010. Geochemical constraints on depth of origin of oceanic carbonatites: The Cape Verde case. Geochim. Cosmochim. Acta 74 (24), 7261–7282.
Ducea, M.N., Currie, C.A., Balica, C., Lazar, I., Mallik, A., Petrescu, L., Vlasceanu, M., 2022. Diapirism of carbonate platforms subducted into the upper mantle. Geology 50 (8), 929–933.
Eggler, D.H., 1978a. Stability of dolomite in a hydrous mantle, with implications for the mantle solidus. Geology 6 (7), 397–400.
Eggler, D.H., 1978b. The effect of CO_2 upon partial melting of peridotite in the system Na_2O-CaO-Al_2O_3-MgO-SiO_2-CO_2 to 35 kb, with an analysis of melting in a peridotite-H2O-CO2 system. Am. J. Sci. 278 (3), 305–343.
Escrig, S., Doucelance, R., Moreira, M., Allègre, C.J., 2005. Os isotope systematics in Fogo Island: evidence for lower continental crust fragments under the Cape Verde Southern Islands. Chem. Geol. 219 (1–4), 93–113.
Esposito, R., 2021. Chapter 7: A protocol and review of methods to select, analyze and interpret melt inclusions to determine preeruptive volatile contents of magmas. In: Lecumberri-Sanchez, P., Steele-MacInnis, M., Kontak, D., (Eds), Fluid and Melt Inclusions: Applications to Geologic Processes. Mineralogical Association of Canada, Topics in Mineral Sciences, Volume 49, pp. 163-194.
Farsang, S., Louvel, M., Zhao, C., Mezouar, M., Rosa, A.D., Widmer, R.N., Feng, X., Liu, J., Redfern, S.A., 2021. Deep carbon cycle constrained by carbonate solubility. Nat. Commun. 12 (1), 4311.
Foley, S.F., Fischer, T.P., 2017. An essential role for continental rifts and lithosphere in the deep carbon cycle. Nat. Geosci. 10 (12), 897–902.
Frezzotti, M.L., Ferrando, S., 2018. The role of halogens in the lithospheric mantle. In: Harlov, D., Aranovich, L. (Eds.), The Role of Halogens in Terrestrial and Extraterrestrial Geochemical Processes. Springer Geochemistry, Springer, Chambridge, pp. 805–845.
Frezzotti, M.L., Touret, J.L., 2014. CO_2, carbonate-rich melts, and brines in the mantle. Geosci. Front. 5 (5), 697–710.
Frezzotti, M.L., 2001. Silicate-melt inclusions in magmatic rocks: applications to petrology. Lithos 55 (1–4), 273–299.
Frezzotti, M.L., Andersen, T., Neumann, E.R., Simonsen, S.L., 2002a. Carbonatite melt–CO_2 fluid inclusions in mantle xenoliths from Tenerife, Canary Islands: a story of trapping, immiscibility and fluid–rock interaction in the upper mantle. Lithos 64 (3–4), 77–96.
Frezzotti, M.L., Touret, J.L., Neumann, E.R., 2002b. Ephemeral carbonate melts in the upper mantle: carbonate-silicate immiscibility in microveins and inclusions within spinel peridotite xenoliths, La Gomera, Canary Islands. Eur. J. Mineral. 14 (5), 891–904.
Frezzotti, M.L., Tecce, F., Casagli, A., 2012. Raman spectroscopy for fluid inclusion analysis. J. Geochem. Explor. 112, 1–20.
Gaillard, F., Malki, M., Iacono-Marziano, G., Pichavant, M., Scaillet, B., 2008. Carbonatite melts and electrical conductivity in the asthenosphere. Science 322 (5906), 1363–1365.
Gerbode, C., Dasgupta, R., 2010. Carbonate-fluxed melting of MORB-like pyroxenite at 2.9 GPa and genesis of HIMU ocean island basalts. J. Petrol. 51 (10), 2067–2088.
Gerlach, D.C., Cliff, R.A., Davies, G.R., Norry, M., Hodgson, N., 1988. Magma sources of the Cape Verdes archipelago: isotopic and trace element constraints. Geochim. Cosmochim. Acta 52 (12), 2979–2992.
Gibson, S.A., McKenzie, D., 2023. On the role of Earth's lithospheric mantle in global volatile cycles. Earth Planet. Sci. Lett. 602, 117946.
Grassi, D., Schmidt, M.W., 2011. The melting of carbonated pelites from 70 to 700 km depth. J. Petrol. 52 (4), 765–789.
Green, D.H., Wallace, M.E., 1988. Mantle metasomatism by ephemeral carbonatite melts. Nature 336 (6198), 459–462.
Grégoire, M., Moine, B.N., O'Reilly, S.Y., Cottin, J.Y., Giret, A., 2000. Trace element residence and partitioning in mantle xenoliths metasomatized by highly alkaline, silicate-and carbonate-rich melts (Kerguelen Islands, Indian Ocean). J. Petrol. 41 (4), 477–509.
Hammouda, T., Laporte, D., 2000. Ultrafast mantle impregnation by carbonatite melts. Geology 28 (3), 283–285.
Hammouda, T., Keshav, S., 2015. Melting in the mantle in the presence of carbon: Review of experiments and discussion on the origin of carbonatites. Chem. Geol. 418, 171–188.
Harris, B.J.R., De Hoog, J.C.M., Halama, R., 2022. The behaviour of nitrogen during subduction of oceanic crust: insights from in situ SIMS analyses of high-pressure rocks. Geochim. Cosmochim. Acta 321, 16–34.
Hart, S.R., 1988. Heterogeneous mantle domains: signatures, genesis and mixing chronologies. Earth Planet. Sci. Lett. 90 (3), 273–296.
Hart, S.R., Hauri, E.H., Oschmann, L.A., Whitehead, J.A., 1992. Mantle plumes and entrainment—Isotopic evidence. Science 256, 517–520.
Hoernle, K., Tilton, G., Le Bas, M.J., Duggen, S., Garbe-Schönberg, D., 2002. Geochemistry of oceanic carbonatites compared with continental carbonatites: mantle recycling of oceanic crustal carbonate. Contribut. Mineral. Petrol. 142 (5), 520–542.
Holm, P.M., Wilson, J.R., Christensen, B.P., Hansen, L., Hansen, S.L., Hein, K.M., Mortensen, A.K., Pedersen, R., Plesner, S., Runge, M.K., 2006. Sampling the Cape Verde mantle plume: evolution of melt compositions on Santo Antão, Cape Verde Islands. J. Petrol. 47 (1), 145–189.
Holm, P.M., Grandvuinet, T., Friis, J., Wilson, J.R., Barker, A.K., Plesner, S., 2008. An ^{40}Ar-^{39}Ar study of the Cape Verde hot spot: Temporal evolution in a semistationary plate environment. J. Geophys. Res. Solid Earth 113, B08201.
Ionov, D.A., O'Reilly, S.Y., Genshaft, Y.S., Kopylova, M.G., 1996. Carbonate-bearing mantle peridotite xenoliths from Spitsbergen: phase relationships, mineral compositions and trace-element residence. Contributi. Mineral. Petrol. 125 (4), 375–392.
Ionov, D.A., Bodinier, J.L., Mukasa, S.B., Zanetti, A., 2002. Mechanisms and sources of mantle metasomatism: major and trace element compositions of peridotite xenoliths from Spitsbergen in the context of numerical modelling. J. Petrol. 43 (12), 2219–2259.
Ionov, D.A., Hofmann, A.W., Merlet, C., Gurenko, A.A., Hellebrand, E., Montagnac, G., Gillet, P., Prikhodko, V.S., 2006. Discovery of whitlockite in mantle xenoliths: Inferences for water-and halogen-poor fluids and trace element residence in the terrestrial upper mantle. Earth Planet. Sci. Lett. 244 (1–2), 201–217.
Jørgensen, J.Ø., Holm, P.M., 2002. Temporal variation and carbonatite contamination in primitive ocean island volcanics from São Vicente, Cape Verde Islands. Chem. Geol. 192 (3–4), 249–267.
Kamenetsky, V.S., Yaxley, G.M., 2015. Carbonate–silicate liquid immiscibility in the mantle propels kimberlite magma ascent. Geochim. Cosmochim. Acta 158, 48–56.
Kelemen, P.B., Manning, C.E., 2015. Re-evaluating carbon fluxes in subduction zones: What goes down, mostly comes up. Proc. Nat. Acad. Sci. 112 (30), E3997–E4006.
Kiseeva, E.S., Yaxley, G.M., Hermann, J., Litasov, K.D., Rosenthal, A., Kamenetsky, V.S., 2012. An experimental study of carbonated eclogite at 3.5–5.5 GPa—implications for silicate and carbonate metasomatism in the cratonic mantle. J. Petrol. 53 (4), 727–759.
Kogarko, L.N., Henderson, C.M.B., Pacheco, H., 1995. Primary Ca-rich carbonatite magma and carbonate-silicate-sulphide liquid immiscibility in the upper mantle. Contribut. Mineral. Petrol. 121 (3), 267–274.
Köhler, T.P., Brey, G., 1990. Calcium exchange between olivine and clinopyroxene calibrated as a geothermobarometer for natural peridotites from 2 to 60 kb with applications. Geochim. Cosmochim. Acta 54 (9), 2375–2388.
Le Maitre, R.W., Streckeisen, A., Zanettin, B., Le Bas, M.J., Bonin, B., Bateman, P., 2002. Igneous Rocks: A Classification and Glossary of Terms: Recommendations of the International Union of Geological Sciences Subcommission on the Systematics of Igneous Rocks. Cambridge University Press, Cambridge, p. 236.
Li, J.L., Schwarzenbach, E.M., John, T., Ague, J.J., Huang, F., Gao, J., Klemd, R., Whitehouse, M.J., Wang, X.S., 2020. Uncovering and quantifying the subduction zone sulfur cycle from the slab perspective. Nat. Commun. 11 (1), 514.
Litasov, K.D., Podgornykh, N.M., 2017. Raman spectroscopy of various phosphate minerals and occurrence of tuite in the Elga IIE iron meteorite. J. Raman Spectros. 48 (11), 1518–1527.
Liu, X., Zhao, D., 2021. Seismic evidence for a plume-modified oceanic lithosphere–asthenosphere system beneath Cape Verde. Geophys. J. Int. 225 (2), 872–886.
Lo Forte, F.M.L., Schiavi, F., Rose-Koga, E.F., Rotolo, S.G., Verdier-Paoletti, M., Aiuppa, A., Zanon, V., 2024a. High CO_2 in the mantle source of ocean island basanites. Geochim. Cosmochim. Acta 368, 93–111.
Lo Forte, F.M.L., Boudoire, G., Frezzotti, M.L., Rotolo, S.G., Sandoval-Velasquez, A., Viveiros, F., Zanon, V., Aiuppa, A., Rizzo, A.L., 2024b. The helium and carbon isotopic signature of Ocean island basalts: Insights from Fogo volcano (Cape Verde archipelago). Earth Planet. Sci. Lett. 645, 118930.
Lodge, A., Helffrich, G., 2006. Depleted swell root beneath the Cape Verde Islands. Geology 34 (6), 449–452.
Lodhia, B.H., Roberts, G.G., Fraser, A.J., Fishwick, S., Goes, S., Jarvis, J., 2018. Continental margin subsidence from shallow mantle convection: Example from West Africa. Earth Planet. Sci. Lett. 481, 350–361.
Luth, R.W., Stachel, T., 2014. The buffering capacity of lithospheric mantle: implications for diamond formation. Contribut. Mineral. Petrol. 168, 1–12.
Madeira, J., Mata, J., Mourão, C., Brum da Silveira, A., Martins, S., Ramalho, R., Hoffmann, D.L., 2010. Volcano-stratigraphic and structural evolution of Brava Island (Cape Verde) based on $^{40}Ar/^{39}Ar$, U-Th and field constraints. J. Volcanol. Geotherm. Res. 196, 219–235.
Maffeis, A., Ferrando, S., Connolly, J.A.D., Frezzotti, M.L., Castelli, D., 2023. Fluid redox fingerprint of the $CaCO_3$ + antigorite dehydration reaction in subducted metacarbonate sediments. Geosciences 13 (5), 130.
Maffeis, A., Frezzotti, M.L., Connolly, J.A.D., Castelli, D., Ferrando, S., 2024. Sulfur disproportionation in deep COHS slab fluids drives mantle wedge oxidation. Sci. Adv. 10 (12), eadj2770.
Malusà, M.G., Frezzotti, M.L., Ferrando, S., Brandmayr, E., Romanelli, F., Panza, G.F., 2018. Active carbon sequestration in the Alpine mantle wedge and implications for long-term climate trends. Sci. Rep. 8 (1), 4740.
Manning, C.E., Frezzotti, M.L., 2020. Subduction-zone fluids. Elements Int. Mag. Mineral. Geochem. Petrol. 16 (6), 395–400.
Martins, S., Mata, J., Munhá, J., Mendes, M.H., Maerschalk, C., Caldeira, R., Mattielli, N., 2010. Chemical and mineralogical evidence of the occurrence of mantle metasomatism by carbonate-rich melts in an oceanic environment (Santiago Island, Cape Verde). Mineral. Petrol. 99, 43–65.
McDonough, W.S., 1990. Constraints on the composition of the continental lithospheric mantle. Earth Planet. Sci. Lett. 101 (1), 1–18.

McKenzie, D.A.N., O'nions, R. K, 1991. Partial melt distributions from inversion of rare earth element concentrations. J. Petrol. 32 (5), 1021–1091.
Mendes, M.H., Caldeira, R., Silva, L., Munhá, J., 2004. Petrology of spinel peridotite xenoliths from Santo Antao, Cape Verde Islands. Comunicações Geológicas 91, 99–116.
Mercier, J.C., Nicolas, A., 1975. Textures and fabrics of upper-mantle peridotites as illustrated by xenoliths from basalts. J. Petrol. 16 (1), 454–487.
Miller, W.G., Maclennan, J., Shorttle, O., Gaetani, G.A., Le Roux, V., Klein, F., 2019. Estimating the carbon content of the deep mantle with Icelandic melt inclusions. Earth Planet. Sci. Lett. 523, 115699.
Mitchell, J.G., Le Bas, M.J., Zielonka, J., Furnes, H., 1983. On dating the magmatism of Maio, Cape Verde Islands. Earth Planet. Sci. Lett. 64, 61–76.
Moine, B.N., Grégoire, M., O'Reilly, S.Y., Delpech, G., Sheppard, S.M.F., Lorand, J.P., Renac, C., Giret, A., Cottin, J.Y., 2004. Carbonatite melt in oceanic upper mantle beneath the Kerguelen Archipelago. Lithos 75 (1–2), 239–252.
Mourão, C., Moreira, M., Mata, J., Raquin, A., Madeira, J., 2012a. Primary and secondary processes constraining the noble gas isotopic signatures of carbonatites and silicate rocks from Brava Island: evidence for a lower mantle origin of the Cape Verde plume. Contribut. Mineral. Petrol. 163, 995–1009.
Mourão, C., Mata, J., Doucelance, R., Madeira, J., Millet, M.-A., Moreira, M., 2012b. Geochemical temporal evolution of Brava Island magmatism: constraints on the variability of Cape Verde mantle sources and on the carbonatite-silicate magma link. Chem. Geol. 334, 44–61.
Neumann, E.R., Simon, N.S., 2009. Ultra-refractory mantle xenoliths from ocean islands: How do they compare to peridotites retrieved from oceanic sub-arc mantle? Lithos 107 (1–2), 1–16.
Nishio, I., Morishita, T., Tamura, A., Itano, K., Takamizawa, S., Ichiyama, Y., Arai, S., Barrett, N., Zilas, K., 2023. Formation of ultra-depleted mantle peridotites and their relationship with boninitic melts: An example from the Kamuikotan Unit, Hokkaido, Japan. J. Geophys. Res. Solid Earth 128 (2), e2022JB025066.
Oliveira, B., Afonso, J.C., Tilhac, R., 2020. A disequilibrium reactive transport model for mantle magmatism. J. Petrol. 61 (9), egaa067.
O'Reilly, S.Y., Zhang, M., Griffin, W.L., Begg, G., Hronsky, J., 2009. Ultradeep continental roots and their oceanic remnants: a solution to the geochemical "mantle reservoir" problem? Lithos 112, 1043–1054.
Palme, H., O'Neill, H. S. T. C., 2014. 3.1 Cosmochemical estimates of mantle composition. In: Holland, H.D., Turekian, K.K. (Eds.), Treatise on Geochemistry (2nd Edition). Volume 3 The Mantle and Core. Elsevier, pp. 1-39.
Pearson, D.G., Canil, D., Shirey, S.B., 2003. Mantle samples included in volcanic rocks: xenoliths and diamonds. Treatise Geochem. 2, 568.
Plank, T., Manning, C.E., 2019. Subducting carbon. Nature 574 (7778), 343–352.
Rudnick, R.L., McDonough, W.F., Chappell, B.W., 1993. Carbonatite metasomatism in the northern Tanzanian mantle: petrographic and geochemical characteristics. Earth Planet. Sci. Lett. 114 (4), 463–475.
Ryabchikov, J.D., Ntaflos, T., Kurat, G., Kogarko, L.N., 1995. Glass-bearing xenoliths from Cape Verde: evidence for a hot rising mantle jet. Mineral. Petrol. 55, 217–237.
Rychert, C.A., Shearer, P.M., 2009. A global view of the lithosphere-asthenosphere boundary. Science 324 (5926), 495–498.
Scambelluri, M., Cannaò, E., Gilio, M., 2019. The water and fluid-mobile element cycles during serpentinite subduction. A review. Eur. J. Mineral. 31 (3), 405–428.
Schmerr, N., 2012. The Gutenberg discontinuity: Melt at the lithosphere-asthenosphere boundary. Science 335 (6075), 1480–1483.
Scott, J.M., Liu, J., Pearson, D.G., Harris, G.A., Czertowicz, T.A., Woodland, S.J., Riches, A.J.V., Luth, R.W., 2019. Continent stabilisation by lateral accretion of subduction zone-processed depleted mantle residues; insights from Zealandia. Earth Planet. Sci. Lett. 507, 175–186.
Sharygin, I.S., Litasov, K.D., Shatskiy, A., Safonov, O.G., Golovin, A.V., Ohtani, E., Pokhilenko, N.P., 2017. Experimental constraints on orthopyroxene dissolution in alkali-carbonate melts in the lithospheric mantle: Implications for kimberlite melt composition and magma ascent. Chem. Geol. 455, 44–56.
Shaw, C.S., Heidelbach, F., Dingwell, D.B., 2006. The origin of reaction textures in mantle peridotite xenoliths from Sal Island, Cape Verde: the case for "metasomatism" by the host lava. Contribut. Mineral. Petrol. 151 (6), 681–697.
Shaw, D.M., 2006. Trace Elements in Magmas: A Theoretical Treatment. Cambridge University Press, Cambridge, p. 243.
Shcheka, S.S., Wiedenbeck, M., Frost, D.J., Keppler, H., 2006. Carbon solubility in mantle minerals. Earth Planet. Sci. Lett. 245 (3–4), 730–742.
Shejwalkar, A., Coogan, L.A., 2013. Experimental calibration of the roles of temperature and composition in the Ca-in-olivine geothermometer at 0.1 MPa. Lithos 177, 54–60.
Silva, L., Serralheiro, A., Macedo, J., Gomes, A., Torres, P., 1990. Carta Geológica de Cabo Verde, Ilha do Sal, na escala de 1/25 000 (folhas 1–2). Instituto Investigação Científica Tropical-Instituto de Cooperação Económica, Lisboa (in Portuguese).
Simon, N.S., Neumann, E.R., Bonadiman, C., Coltorti, M., Delpech, G., Grégoire, M., Widom, E., 2008. Ultra-refractory domains in the oceanic mantle lithosphere sampled as mantle xenoliths at ocean islands. J. Petrol. 49 (6), 1223–1251.
Stagno, V., Frost, D.J., 2010. Carbon speciation in the asthenosphere: Experimental measurements of the redox conditions at which carbonate-bearing melts coexist with graphite or diamond in peridotite assemblages. Earth Planet. Sci. Lett. 300 (1–2), 72–84.
Stagno, V., Ojwang, D.O., McCammon, C.A., Frost, D.J., 2013. The oxidation state of the mantle and the extraction of carbon from Earth's interior. Nature 493 (7430), 84–88.
Stone, R.S., Luth, R.W., 2016. Orthopyroxene survival in deep carbonatite melts: implications for kimberlites. Contribut. Mineral. Petrol. 171, 1–9.
Stracke, A., Bizimis, M., Salters, V.J., 2003. Recycling oceanic crust: Quantitative constraints. Geochem. Geophys. Geosyst. 4 (3), 8003.
Sun, S.S., 1982. Chemical composition and origin of the Earth's primitive mantle. Geochim. Cosmochim. Acta 46 (2), 179–192.
Sun, C., Dasgupta, R., 2023. Carbon budget of Earth's deep mantle constrained by petrogenesis of silica-poor ocean island basalts. Earth Planet. Sci. Lett. 611, 118135.
Takahashi, E., 1986. Origin of basaltic magmas—implications from peridotite melting experiments and an olivine fractionation model. Bull. Volcanol. Soc. Japan 30, S17–S40 (in Japanese with English abstract).
Tamburello, G., Pondrelli, S., Chiodini, G., Rouwet, D., 2018. Global-scale control of extensional tectonics on CO_2 Earth degassing. Nat. Commun. 9 (1), 4608.
Thomsen, T.B., Schmidt, M.W., 2008. Melting of carbonated pelites at 2.5–5.0 GPa, silicate–carbonatite liquid immiscibility, and potassium–carbon metasomatism of the mantle. Earth Planet. Sci. Lett. 267 (1–2), 17–31.
Tomlinson, E.L., Holland, T.J., 2021. A thermodynamic model for the subsolidus evolution and melting of peridotite. J. Petrol. 62 (1), egab012.
Torres, P.C., Silva, L.C., Serralheiro, A., Tassinari, C., Munhá, J., 2002. Enquadramento geocronológico pelo método K/Ar das principais sequências vulcano-estratigráficas da Ilha do Sal – Cabo Verde. Garcia de Orta. Série de Geologia 18 (1–2), 9–13 (in Portuguese).
Torres, P., Silva, L.D., Munhá, J., Caldeira, R., Mata, J., Tassinari, C.C.G., 2010. Petrology and geochemistry of lavas from Sal Island: implications for the variability of the Cape Verde magmatism. Comun. Geol. 97, 35–61.
Tsuno, K., Dasgupta, R., 2011. Melting phase relation of nominally anhydrous, carbonated pelitic-eclogite at 2.5–3.0 GPa and deep cycling of sedimentary carbon. Contribut. Mineral. Petrol. 161, 743–763.
Uenver-Thiele, L., Woodland, A.B., Seitz, H.M., Downes, H., Altherr, R., 2017. Metasomatic processes revealed by trace element and redox signatures of the lithospheric mantle beneath the Massif Central, France. J. Petrol. 58 (3), 395–422.
Villaseca, C., Orejana, D., Huertas, M.J., Ancochea, E., de Ignacio, C., Mata, J., Caldeira, R., García-Rodríguez, M., Moreno, J.A., Pérez-Sob, C., 2025. The old central igneous complexes of Sal, Boa Vista and Maio islands: Implications for 17 Ma of isotopic evolution of the Cape Verde archipelago. Lithos 498–499, 107975.
Villeneuve, M., Gärtner, A., Mueller, P. A., Guillou, O., Linnemann, U., 2024. Colliding cratons: linking the Variscan orogeny in West Africa and North America. In: Nance, R.D., Strachan, R.A., Quesada, C., Lin, S. (Eds.), Supercontinents, Orogenesis and Magmatism. Geol. Soc. London Spe. Publ. 542, 359-377.
Villeneuve, M., Marcaillou, B., 2013. Pre-Mesozoic origin and paleogeography of blocks in the Caribbean, South Appalachian and West African domains and their impact on the post "variscan" evolution. Bull. Societe Geol. France 184 (1-2), 5–20.
Vinnik, L., Silveira, G., Kiselev, S., Farra, V., Weber, M., Stutzmann, E., 2012. Cape Verde hotspot from the upper crust to the top of the lower mantle. Earth Planet. Sci. Lett. 319, 259–268.
Viti, C., Frezzotti, M.L., 2001. Transmission electron microscopy applied to fluid inclusion investigations. Lithos 55 (1–4), 125–138.
Wilson, D.J., Peirce, C., Watts, A.B., Grevemeyer, I., Krabbenhöft, A., 2010. Uplift at lithospheric swells—I: seismic and gravity constraints on the crust and uppermost mantle structure of the Cape Verde mid-plate swell. Geophys. J. Int. 182 (2), 531–550.
Winter, J.D., 2014. Principles of Igneous and Metamorphic Petrology, 2. UK Pearson Education, Harlow.
Wojdyr, M., 2010. Fityk: a general-purpose peak fitting program. Appl. Crystallograp. 43 (5), 1126–1128.
Wong, K., Mason, E., Brune, S., East, M., Edmonds, M., Zahirovic, S., 2019. Deep carbon cycling over the past 200 million years: a review of fluxes in different tectonic settings. Front. Earth Sci. 7, 263.
Workman, R.K., Hart, S.R., 2004. Major and trace element composition of the depleted MORB mantle (DMM). Earth Planet. Sci. Lett. 231 (1–2), 53–72.
Wu, S., Wörner, G., Jochum, K.P., Stoll, B., Simon, K., Kronz, A., 2019. The preparation and preliminary characterisation of three synthetic andesite reference glass materials (ARM-1, ARM-2, ARM-3) for in situ microanalysis. Geostandard. Geoanalyt. Res. 43 (4), 567–584.
Yaxley, G.M., Crawford, A.J., Green, D.H., 1991. Evidence for carbonatite metasomatism in spinel peridotite xenoliths from western Victoria, Australia. Earth Planet. Sci. Lett. 107 (2), 305–317.
Yaxley, G.M., Green, D.H., Kamenetsky, V., 1998. Carbonatite metasomatism in the southeastern Australian lithosphere. J. Petrol. 39 (11–12), 1917–1930.
Yaxley, G.M., Anenburg, M., Tappe, S., Decree, S., Guzmics, T., 2022. Carbonatites: classification, sources, evolution, and emplacement. Ann. Rev. Earth Planet. Sci. 50 (1), 261–293.
Zhao, S., Schettino, E., Merlini, M., Poli, S., 2019. The stability and melting of aragonite: An experimental and thermodynamic model for carbonated eclogites in the mantle. Lithos 324, 105–114.